Composite Structures 163 (2017) 216–237

Contents lists available at ScienceDirect

Composite Structures

journal homepage: www.elsevier.com/locate/compstruct

Static studies of stepped functionally graded magneto-electro-elastic beam subjected to different thermal loads

M. Vinyas, S.C. Kattimani *

Department of Mechanical Engineering, National Institute of Technology Karnataka, Surathkal 575025, India

ARTICLE INFO

Article history:
Received 4 November 2016
Accepted 9 December 2016
Available online 12 December 2016

Keywords:
Stepped functionally graded (SFG)
Pyroeffects
Magneto-electro-elastic
Temperature distribution
Direct and derived quantities

ABSTRACT

In this article, a three dimensional finite element (FE) formulation for a multilayered magneto-electro-elastic (MEE) beam in thermal environment is presented. The equilibrium equations of the system are attained using the principle of total potential energy and linear coupled constitutive equations of MEE material. The corresponding FE equations are derived and the numerical evaluation of stepped functionally graded (SFG) MEE beam is carried out. The influence of various in-plane and through thickness temperature distributions on the direct quantities (displacements and potentials) and derived quantities (stresses, electric displacement and magnetic flux density), across the thickness of SFG-MEE cantilever beam is analyzed. In addition, an attempt has been made to investigate the effect of stacking sequence, thermo-magnetic and thermo-electric coupling on the direct quantities of the SFG-MEE beam. Further, a comparative study is made to evaluate the variations of displacements, potentials, electric displacements, magnetic flux density and stresses at different regions of the beam. It is expected that the results presented in this article may be useful in the design and analysis of MEE smart structures and sensor applications.

1. Introduction

The development of smart structures made of magneto-electro-elastic (MEE) materials offers a great potential for their use in many advanced structural applications. This class of material displays a unique self responsive and self controllable property. Further, the MEE materials exhibit a simultaneous coupling between the mechanical, electric, magnetic and thermal fields which makes the energy conversion feasible among these forms. These coupling effects are noticed in the macroscopic composite, but are absent in individual phase. The adverse effect of the applied mechanical load is hindered by the strains developed due to magneto-electric load. This reduces the excess utilization of the material and makes the structure light-weighted. The predominant use of these materials is found in the field of sensors and actuators which are usually exposed to high temperature environments. More often, the temperature variations serves as a contributing factor in predicting the performance of the structure. Hence, the study of influence of various temperature distributions on the behavior of MEE structure is an area of concern. It is necessary to accurately evaluate the performance of MEE structures in thermal environment for practical applications. Many pioneers have contributed their research on analyzing the static and free vibration behavior of MEE structures (beams, plates and shells). The predominant computational techniques like approximate solution method, analytical method, state space approach, finite element (FE) method etc., have been adopted to study the characteristic behavior of these structures. Pan and Heyliger [1] derived an analytical solution to evaluate the free vibrations of simply supported multilayered MEE plate. Sladek et al. [2] developed a mesh less method to examine the dynamic problems of thick MEE plates. Ramirez et al. [3] considered the free vibration problem of 2D MEE plates and presented an approximate solution to investigate its fundamental behavior. Milazzo et al. [4] presented an analytical solution to investigate the free and forced vibration of multiphase and laminated MEE beams. Recently, Kattimani and Ray developed the FE formulation for the active control of geometrically nonlinear vibrations of MEE plates [5] and doubly curved shells [6]. They also extended their study for functionally graded MEE plates [7]. Bhangale et al. [8] adopted a semi analytical FE procedure to investigate the free vibration characteristics of the functionally graded MEE plates. Vaezi et al. [9] studied the free vibration of MEE microbeam and the critical potential values resulting in the buckling of the beam are evaluated. The semi analytical state space approach

* Corresponding author.
E-mail address: sck@nitk.ac.in (S.C. Kattimani).

http://dx.doi.org/10.1016/j.compstruct.2016.12.040
0263-8223/

was used by Xin and Hu [10] to investigate the free vibration behavior of layered MEE beams. Ray et al. [11] developed a FE model for the static analysis of simply supported rectangular plate using higher order shear deformation (HSDT) theory. Lage et al. [12] studied the static behavior of MEE plate with the aid of mixed layerwise FE formulation. Biju et al. [13] used magnetic vector potential approach to compute the transient dynamic response of MEE sensors bonded to mild steel beam. Further, they investigated the effect of volume fractions on the potentials of the system. Using the finite element methods, the behavior of MEE sensors subjected to transient mechanical loading is studied by Daga et al. [14]. Apart from FE methods, state space approach was also used to analyze the free vibration and static behavior of MEE plates [15–17]. Phoenix et al. [18] performed the static and dynamic analysis of the coupled MEE plates using the Reissner mixed variational theorem. Research is also devoted to develop the micro-mechanics model to evaluate the effective properties of a piezo-magneto-thermo-elastic composite structure [19–24].

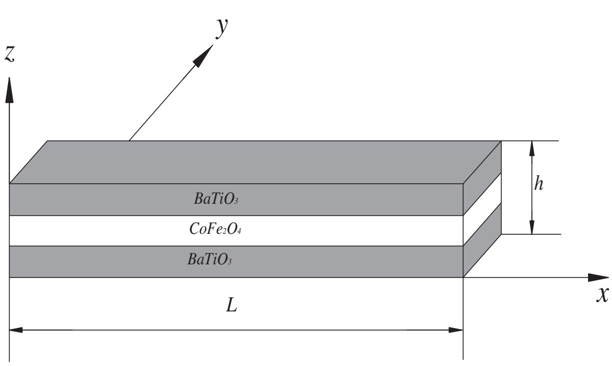

Fig. 1. Multilayered MEE beam.

More often, MEE structures are exposed to various high temperature fluctuations which may induce larger thermo elastic stresses. This consequently alters the performance of these structures when used in the field of sensor and actuators. Further, in thermal environment MEE materials displays an additional coupling between thermo-magnetic and thermo-electric material properties. This unique property can exhibit a significant influence on the potential, electric displacement and magnetic flux density. It is believed that for the precise design and development of MEE structures, it is necessary to consider the effects of various thermal fields along with the other coupling properties. Some of the research articles which motivated in this regard are Panda and Ray [25] studied the nonlinear static FE analysis of functionally graded (FG) plates in thermal environment. Kumaravel et al. [26] evaluated the free vibration and linear buckling of MEE beam under thermal environment. They also investigated the static behavior of MEE strip subjected to uniform and non-uniform temperature loads [27]. Kondaiah et al. [28] studied the behavior of MEE beams subjected to uniform temperature considering the pyroelectric and pyromagnetic effects. Further, the same study was extended to MEE plates also [29]. Carrera et al. [30] analyzed the thermo mechanical response of multilayered plate subjected to various temperature distributions. Also, they have studied a comparison between the classical and the advanced theories. Sunar et al. [31] made use of the thermodynamic potential and derived a FE formulation for fully coupled thermopiezomagnetic continuum. Badri and Kayiem [32] adopted the first order shear deformation theory (FSDT) to analyze the static and dynamic

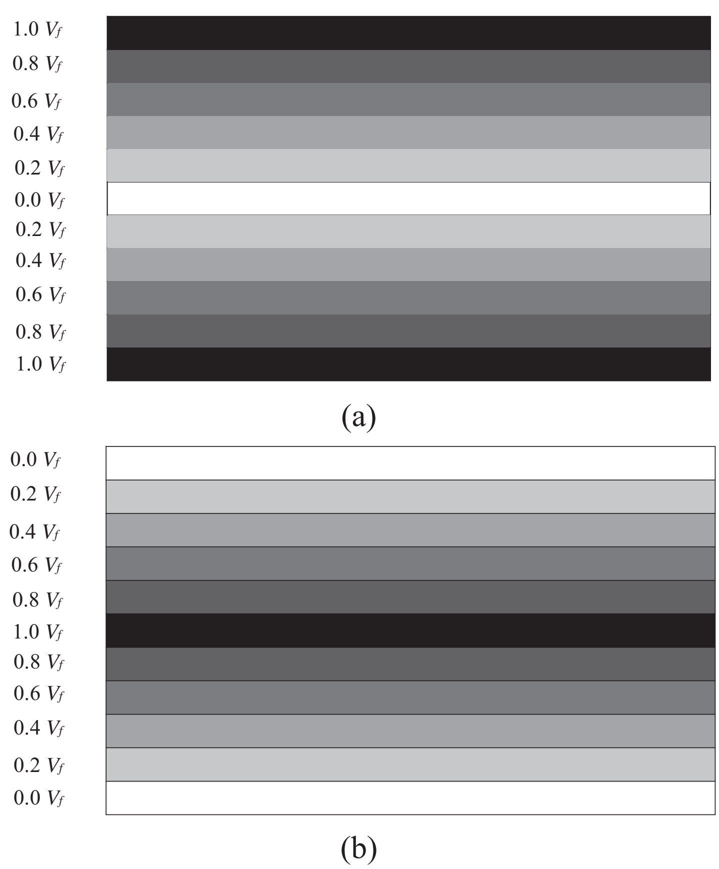

Fig. 2. Stepped functionally graded (a) BFB (b) FBF stacking sequence.

analysis of magneto-thermo-electro-elastic (MTEE) plates. Tauchert [33] developed an exact solution for piezo thermo-elastic problem subjected to steady state temperature distribution. Ebrahimi and Barati [34] analyzed the influence of the various forms of temperature distributions on the frequency characteristics of magneto-electro-thermo-elastic functionally graded (METE-FG) nano beams using the third order shear deformation theory. They also studied the thermo-electro-mechanical buckling behavior of functionally graded piezoelectric materials [35].

To the best of author's knowledge, literature reveals only limited understanding of the behavior of MEE beam in thermal environment. Hence, in the present article, authors have attempted to make comprehensive study of the behavior of stepped functionally graded magneto-electro-elastic (SFG-MEE) beam subjected to various temperature profiles. A finite element formulation of SFG-MEE beam is developed to study the static analysis in thermal environment. The influence of stacking sequence, pyroeffects and temperature profiles on the displacements, potentials and stresses are analyzed. In addition, the variation of direct and derived quantities at different beam regions is evaluated.

2. Problem description

A schematic diagram of multilayered MEE beam consisting of three layers is shown in Fig. 1. The top layer and the bottom layer of the beam being purely piezoelectric whereas the middle layer is of purely piezomagnetic. The Cartesian co-ordinate system is considered at the bottom left corner of the beam. The beam length L is taken along the x-coordinate while the width w and the thickness h are taken along the y- and z-coordinates, respectively. The boundary conditions employed for the cantilever MEE beam are given as follows:

$$u = v = w = \phi = \psi = 0 \text{at} x = 0 \text{ and } u = v = w = \phi = \psi \neq 0 \text{ at } x = L$$

2.1. Stepped functionally graded (SFG) MEE beam

A layerwise or stepped functionally graded magneto-electro-elastic (SFG-MEE) beam is modeled by assigning each layer of the multilayered MEE beam with the material properties corresponding to different volume fraction of Barium Titanate ($BaTiO_3$) and Cobalt Ferric Oxide ($CoFe_2O_4$) [28]. Two different layup sequences namely, layerwise SFG-BFB and SFG-FBF are considered for the analysis. The layerwise SFG-BFB refers to the stacking sequence in which the top and bottom layers are made of pure piezoelectric (PE) phase. The volume fraction of the consecutive layers is varied in steps of $V_f = 0.2$ from both the ends to attain pure piezomagnetic (PM) phase at the middle layer as shown in Fig. 2 (a). Similarly, the SFG-FBF is obtained by replacing the pure PE phase by pure PM phase and increasing the volume fraction of the consecutive layers by 0.2 to attain pure PE phase at the mid layer as depicted in Fig. 2(b).

2.2. Constitutive equations

The linearly coupled constitutive relations for the multilayered thermo-magneto-electro-elastic solid beam can be written as

$$\{\sigma^k\} = [C^k_{V_f}]\{\varepsilon^k\} - [e^k_{V_f}]\{E^k\} - [q^k_{V_f}]\{H^k\} - [C^k_{V_f}]\{\alpha^k_{V_f}\}\Delta T \tag{1.a}$$

$$\{D^k\} = [e^k_{V_f}]^T\{\varepsilon^k\} + [\eta^k_{V_f}]\{E^k\} + [m^k_{V_f}]\{H^k\} + \{p^k_{V_f}\}\Delta T \tag{1.b}$$

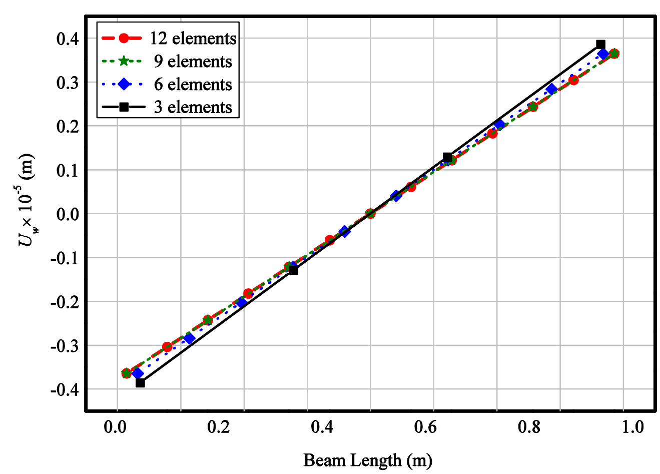

Fig. 3. Convergence of transverse displacement component U_w.

Table 1
Material properties of $BaTiO_3$-$CoFe_2O_4$ composite w.r.t different volume fraction V_f of $BaTiO_3$–$CoFe_2O_4$ (Kondaiah et al. [28]).

Material property	Material constants	0 V_f	0.2 V_f	0.4 V_f	0.5 V_f	0.6 V_f	0.8 V_f	1 V_f
Elastic constants (GPa)	$C_{11} = C_{22}$	286	250	225	220	200	175	166
	C_{12}	173	146	125	120	110	100	77
	$C_{13} = C_{23}$	170	145	125	120	110	100	78
	C_{33}	269.5	240	220	215	190	170	162
	$C_{44} = C_{55}$	45.3	45	45	45	45	50	43
	C_{66}	56.5	52	50	50	45	37.5	44.5
Piezoelectric constants (C/m^2)	e_{31}	0	−2	−3	−3.5	−3.5	−4	−4.4
	e_{33}	0	4	7	9.0	11	14	18.6
	e_{15}	0	0	0	0	0	0	11.6
Dielectric constant (10^{-9} C^2/Nm^2)	$\eta_{11} = \eta_{22}$	0.08	0.33	0.8	0.85	0.9	1	11.2
	η_{33}	0.093	2.5	5	6.3	7.5	10	12.6
Magnetic permeability (10^{-4} Ns^2/C^2)	$\mu_{11} = \mu_{22}$	−5.9	−3.9	−2.5	−2.0	−1.5	−0.8	0.05
	μ_{33}	1.57	1.33	1	0.9	0.75	0.5	0.1
Piezomagnetic constants (N/Am)	q_{31}	580	410	300	350	200	100	0
	q_{33}	700	550	380	320	260	120	0
	q_{15}	560	340	220	200	180	80	0
Magneto-electric constant (10^{-12} Ns/VC)	$m_{11} = m_{22}$	0	2.8	4.8	5.5	6	6.8	0
	m_{33}	0	2000	2750	2600	2500	1500	0
Pyroelectric-constant (10^{-7} C/m^2 K)	p_2	0	−3.5	−6.5	−7.8	−9	−10.8	0
Pyromagnetic constant (10^{-5} C/m^2 K)	τ_2	0	−36	−28	−23	−18	−8.5	0
Thermal expansion coefficient (10^{-6} K^{-1})	$\alpha_1 = \alpha_2$	10	10.8	11.8	12.3	12.9	14.1	15.7
	α_3	10	9.3	8.6	8.2	7.8	7.2	6.4
Density (kg/m^3)	ρ	5300	5400	5500	5550	5600	5700	5800

$$\{B^k\} = [q^k_{V_f}]^T\{\varepsilon^k\} + [m^k_{V_f}]\{E^k\} + [\mu^k_{V_f}]\{H^k\} + \{\tau^k_{V_f}\}\Delta T \tag{1.c}$$

where $[C^k_{V_f}]$, $[e^k_{V_f}]$, $[q^k_{V_f}]$, and $\{\alpha^k_{V_f}\}$ are the elastic co-efficient matrix, the piezoelectric coefficient matrix, the magnetostrictive coefficient matrix and the thermal expansion co-efficient matrix, respectively; $[\eta^k_{V_f}]$, $[m^k_{V_f}]$, $\{p^k_{V_f}\}$, $\{\tau^k_{V_f}\}$ and $[\mu^k_{V_f}]$ are the dielectric constant, electromagnetic coefficient, pyroelectric constant, pyro-magnetic constant and the magnetic permeability constant,

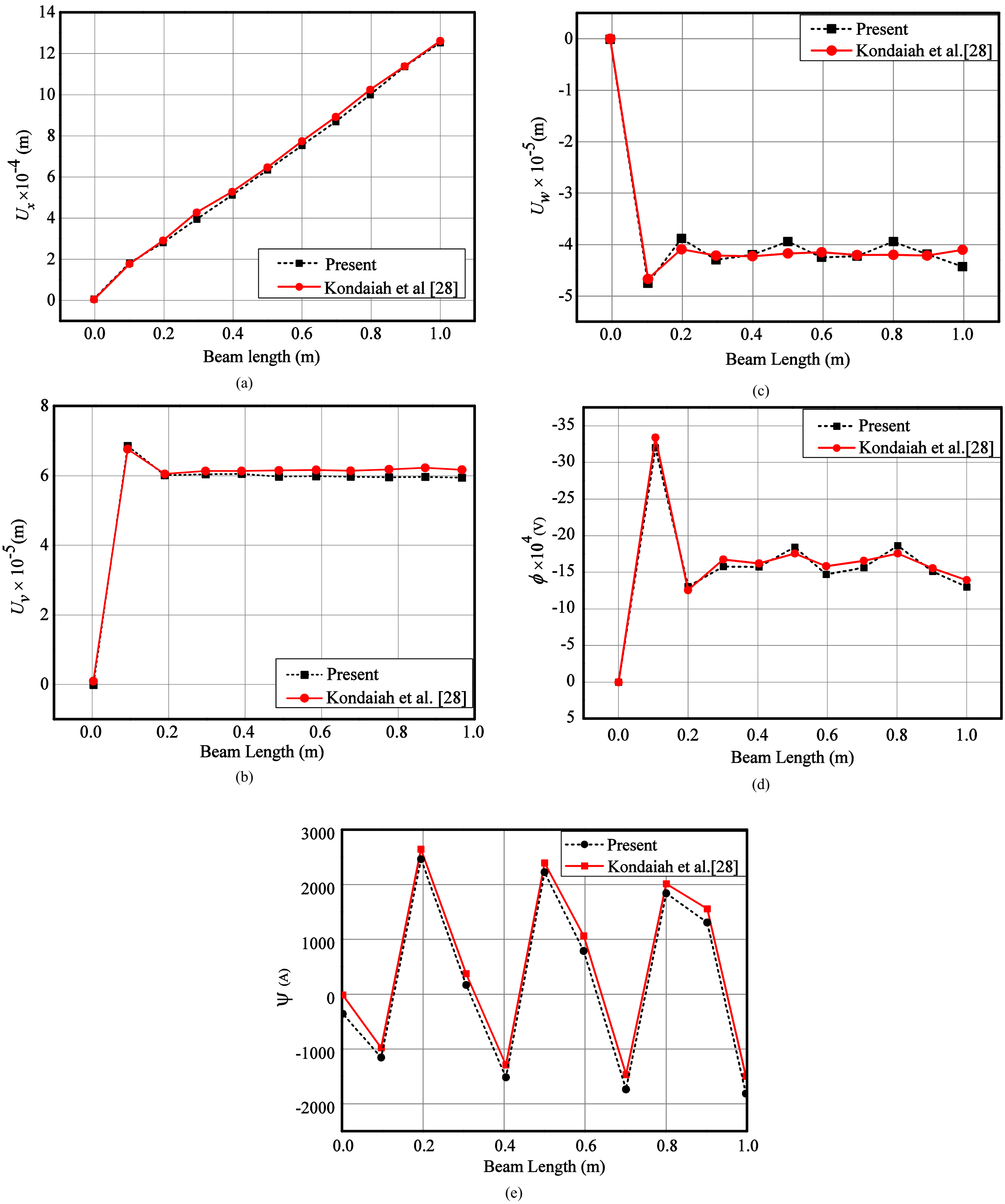

Fig. 4. Validation of (a) longitudinal x-direction (U_x) (b) y-direction (U_v) (c) transverse z-direction (U_w) displacement components (d) electric potential (ϕ) (e) magnetic potential (ψ).

respectively; $\{\sigma^k\}$, $\{D^k\}$ and $\{B^k\}$, represent the stress tensor, electric displacement and the magnetic flux, respectively; $\{\varepsilon^k\}$, $\{E^k\}$, $\{H^k\}$ and ΔT are the linear strain tensor, electric field, magnetic field and temperature rise from a stress free state, respectively. In the above terms k represents the layer number and the subscript V_f denotes the volume fraction of Barium Titanate ($BaTiO_3$) and Cobalt Ferric oxide ($CoFe_2O_4$) corresponding to the kth layer.

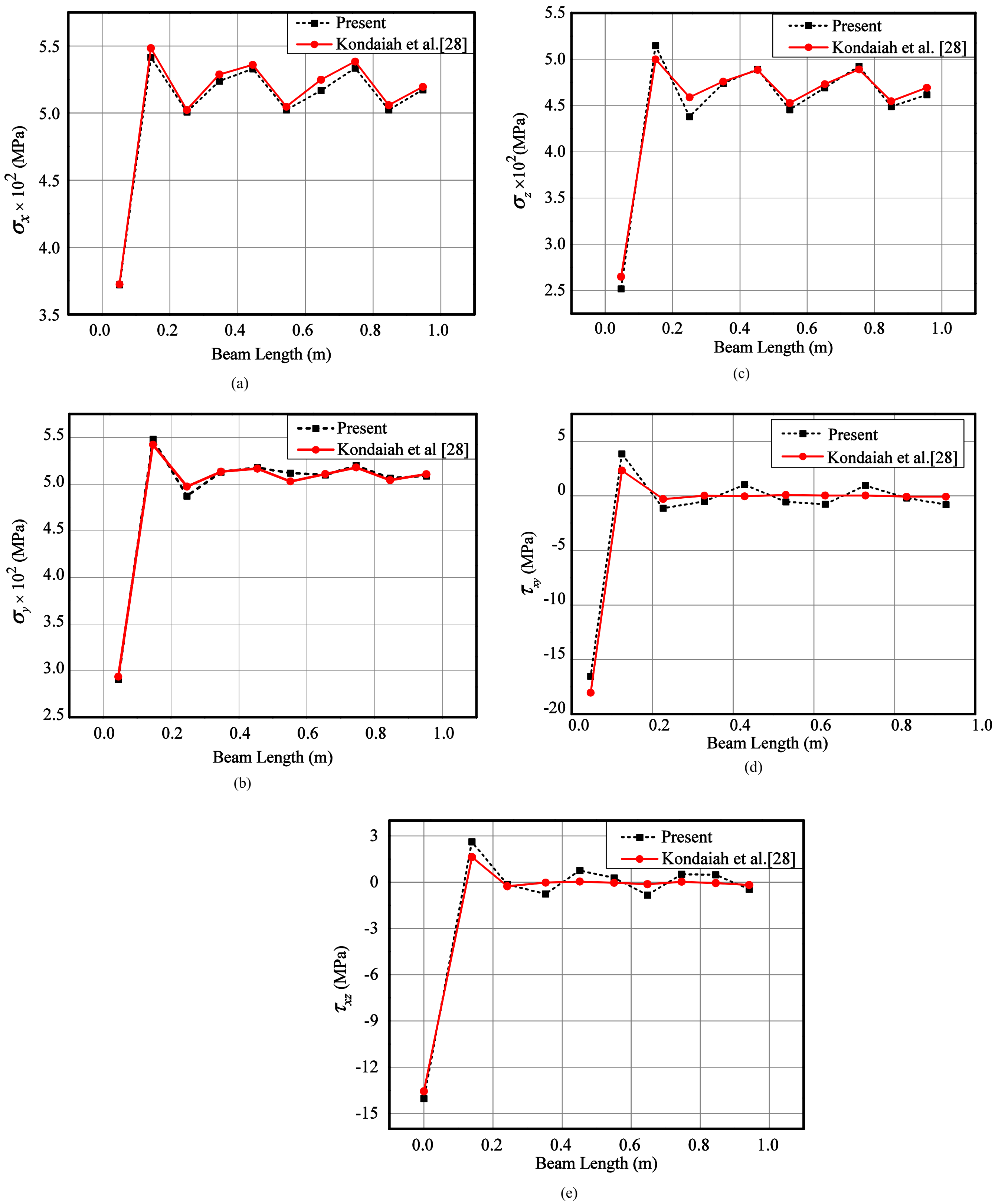

Fig. 5. Validation of (a) normal stress – σ_x (b) normal stress – σ_y (c) normal stress – σ_z (d) shear stress – τ_{xy} (e) shear stress – τ_{xz}.

2.3. Finite element formulation

The magneto-electro-elastic beam is discretized by eight noded brick element with five degree of freedom at each node. At any point within the element, the generalized displacement vector $\{d_t\}$, the electric potential vector $\{\phi\}$ and the magnetic potential vector $\{\psi\}$ can be expressed in terms of the nodal generalized displacement vector $\{d_t^e\}$, the nodal electric potential vector and the nodal magnetic potential vector $\{\psi^e\}$, respectively as follows:

$$\{d_t\} = [N_t]\{d_t^e\}, \{\phi\} = [N_\phi]\{\phi^e\}, \{\psi\} = [N_\psi]\{\psi^e\} \tag{2}$$

in which

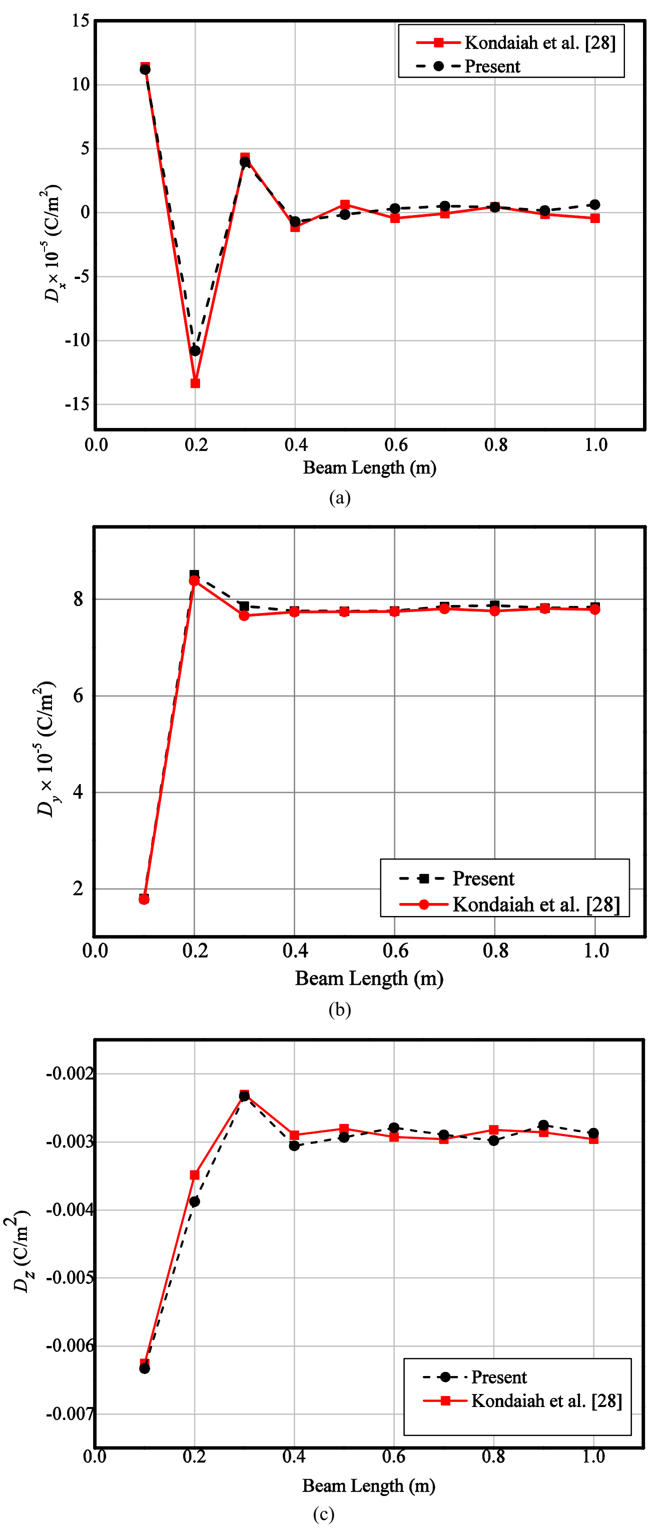

Fig. 6. Validation of electric displacement components (a) D_x (b) D_y (c) D_z.

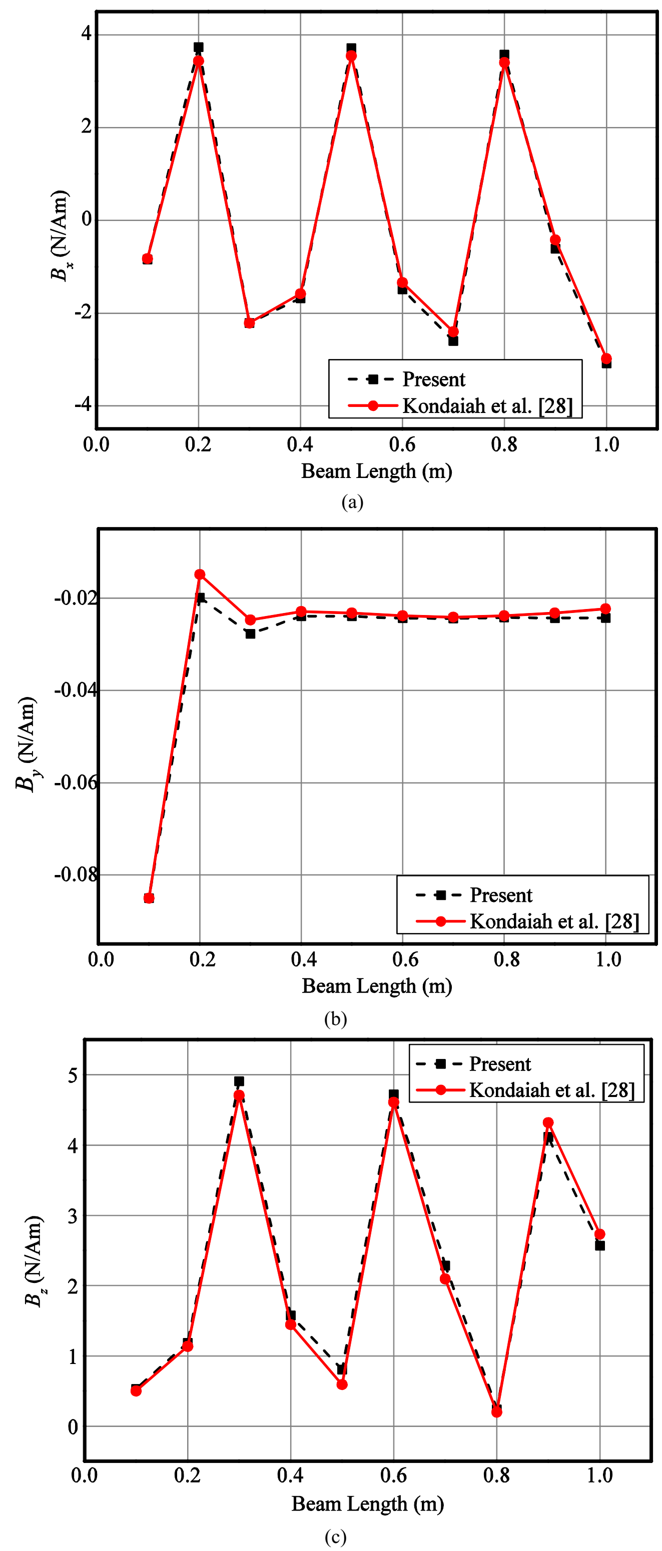

Fig. 7. Validation of magnetic flux density components (a) D_x (b) D_y (c) D_z.

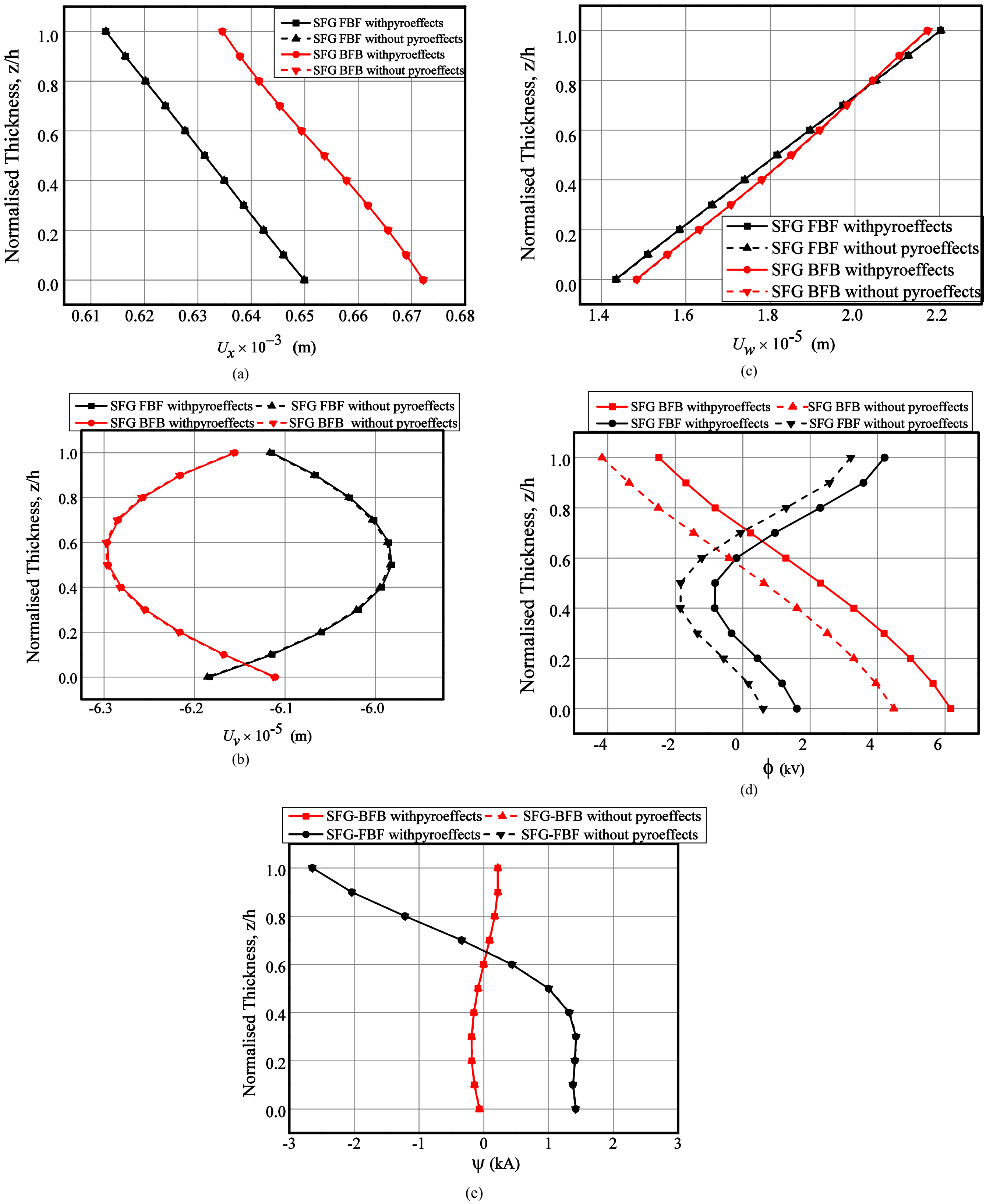

Fig. 8. Variation of (a) longitudinal x-direction displacement component U_x (b) y-direction displacement component U_v (c) z-direction displacement component U_w (d) electric potential ϕ (e) magnetic potential ψ for SFG-BFB and SFG-FBF subjected to uniform temperature load.

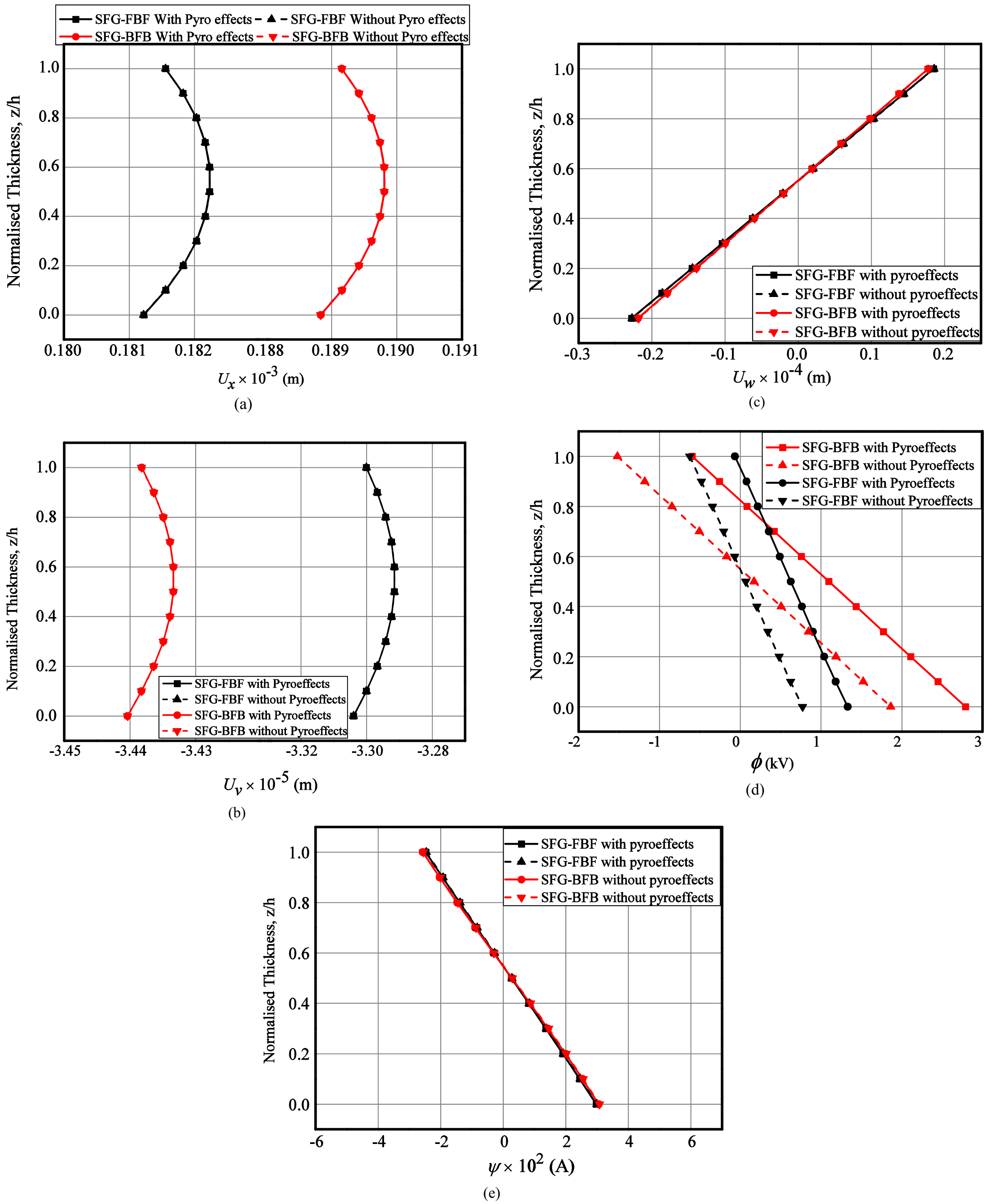

Fig. 9. Variation of (a) longitudinal x-direction displacement component U_x (b) y-direction displacement component U_v (c) z-direction displacement component U_w (d) electric potential ϕ (e) magnetic potential ψ for SFG-BFB and SFG-FBF subjected to linear temperature load.

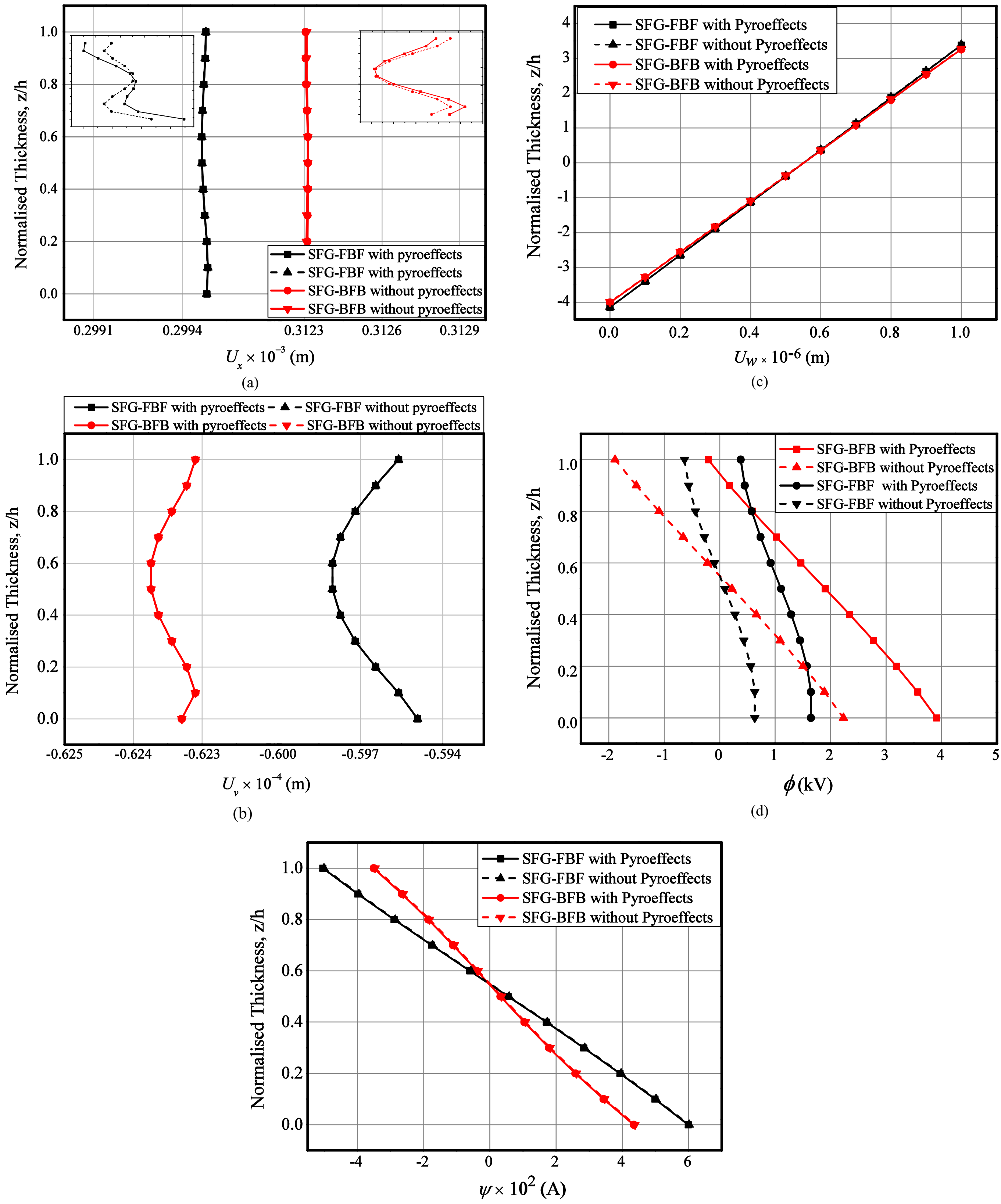

Fig. 10. Variation of (a) longitudinal x-direction displacement component U_x (b) y-direction displacement component U_v (c) z-direction displacement component U_w (d) electric potential ϕ (e) magnetic potential ψ for SFG-BFB and SFG-FBF subjected to sinusoidal temperature load.

$$\{d_t^e\} = \left[\{d_{t1}\}^T\{d_{t2}\}^T\ldots\{d_{t8}\}^T\right]^T, \{\phi^e\} = [\phi_1\phi_2\ldots\phi_8]^T, \{\psi^e\} = [\psi_1\psi_2\ldots\psi_8]^T,$$
$$[N_t] = [N_{t1}N_{t2}\ldots N_{t8}], N_{ti} = n_iI_t, [N_\phi] = [n_1n_2\ldots n_8], [N_\psi] = [n_1n_2\ldots n_8] \tag{3}$$

where n_i is the natural coordinate shape function associated with the ith node of the element; 'I_t' is the identity matrix; $[N_t]$, $[N_\phi]$ and $[N_\psi]$ are (3×24), (1×8) and (1×8) shape function matrices, respectively.

Using the Maxwell's fundamental electrostatic equations, the linear relation between the electric field and the electric potential can be expressed as

$$\{E\} = \left\{-\frac{\partial\phi}{\partial x}, -\frac{\partial\phi}{\partial y}, -\frac{\partial\phi}{\partial z}\right\} \tag{4a}$$

Similarly, the magnetic field and the magnetic potential is related as

$$\{H\} = \left\{-\frac{\partial\psi}{\partial x}, -\frac{\partial\psi}{\partial y}, -\frac{\partial\psi}{\partial z}\right\} \tag{4b}$$

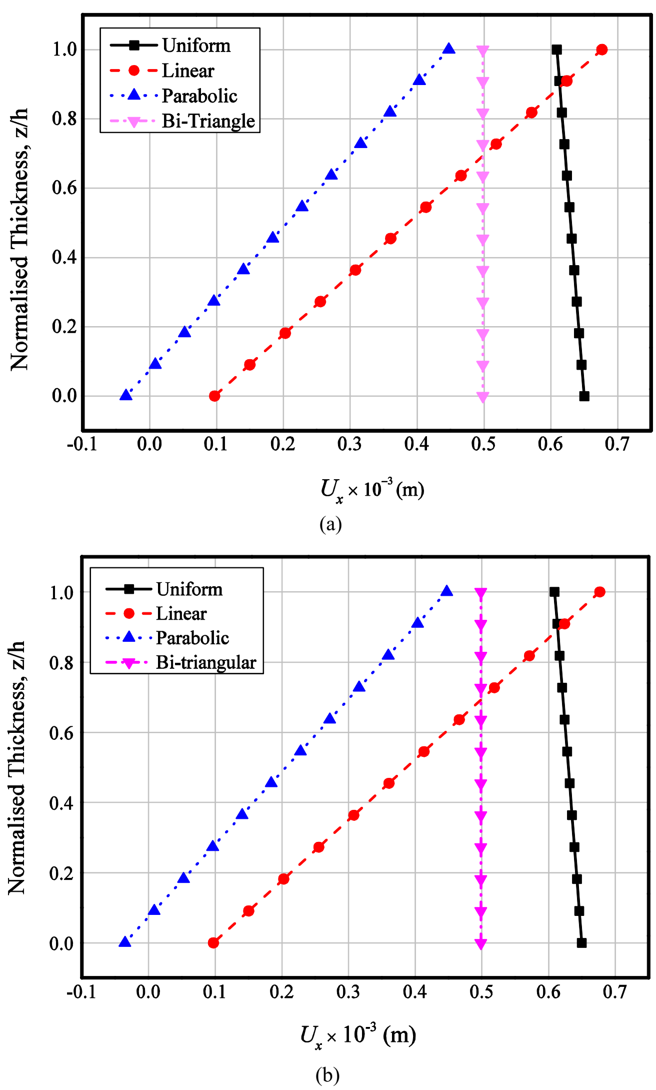

Fig. 11. Effect of various through thickness varying temperature profiles on longitudinal x-direction displacement component U_x (a) SFG-BFB (b) SFG-FBF.

The various derivatives of shape function matrices can be expressed as

$$\{\varepsilon\} = [B_t]\{d_t^e\},\ \{H\} = [B_\psi]\{\psi^e\},\ \{E\} = [B_\phi]\{\phi^e\} \tag{5}$$

Using the derivative of shape function matrices, the strain vector, electric potential vector and magnetic potential vector of the system are expressed in terms of the nodal displacement, nodal electric potential and nodal magnetic potential, respectively as follows:

$$\begin{aligned}\{\varepsilon\} &= L_t\{d_t\} = [L_tN_t]\{d_t^e\} = [B_t]\{d_t^e\},\ \{H\} = L_\psi\{\psi\} = [L_\psi N_\psi]\{\psi^e\} \\ &= [B_\psi]\{\psi^e\}, \{E\} = L_\phi\{\phi\} = [L_\phi N_\phi]\{\phi^e\} = [B_\phi]\{\phi^e\}\end{aligned} \tag{6}$$

where L_t, L_ψ and L_ϕ are the differential operators and the sub matrices $[B_t]$, $[B_\psi]$ and $[B\phi]$ are generally expressed as

$$[B_{ti}] = \begin{bmatrix} \frac{\partial n_i}{\partial x} & 0 & 0 \\ 0 & \frac{\partial n_i}{\partial y} & 0 \\ 0 & 0 & \frac{\partial n_i}{\partial z} \\ 0 & \frac{\partial n_i}{\partial z} & \frac{\partial n_i}{\partial y} \\ \frac{\partial n_i}{\partial z} & 0 & \frac{\partial n_i}{\partial x} \\ \frac{\partial n_i}{\partial y} & \frac{\partial n_i}{\partial x} & 0 \end{bmatrix},\ [B_{\psi i}] = \begin{bmatrix} \frac{-\partial n_i}{\partial x} \\ -\frac{\partial n_i}{\partial y} \\ -\frac{\partial n_i}{\partial z} \end{bmatrix},\ [B_{\phi i}] = \begin{bmatrix} \frac{-\partial n_i}{\partial x} \\ -\frac{\partial n_i}{\partial y} \\ -\frac{\partial n_i}{\partial z} \end{bmatrix} \tag{7}$$

where $i = 1, 2, 3, \ldots, 8$ represents the node number.

2.4. Equations of motion

The principle of total potential energy is invoked to derive the governing equations of the magneto-electro-elastic (MEE) beam in thermal environment as follows:

$$\begin{aligned}T_p = &\frac{1}{2}\sum_{k=1}^{N}\int_{\Omega^k}\{\varepsilon^k\}^T\{\sigma^k\}d\Omega^k - \frac{1}{2}\sum_{k=1}^{N}\int_{\Omega^k}[E^k]^T\{D^k\}d\Omega^k \\ &-\frac{1}{2}\sum_{k=1}^{N}\int_{\Omega^k}[H^k]^T\{B^k\}d\Omega^k - \int_A\{d_t\}^T\{F_{surface}\}dA \\ &-\int_{\Omega^k}\{d_t\}^T\{F_{body}\}d\Omega^k - \{d_t\}^T\{F_{conc}\} - \int_A\phi Q^\phi dA - \int_A\psi Q^\psi dA\end{aligned} \tag{8}$$

where $k = 1, 2, 3, \ldots, N$ represents the number of layers and Ωk denotes the volume of the kth layer. $\{F_{surface}\}$ is the surface force acting over the area A of the layer, $\{F_{body}\}$ is the body force and $\{F_{conc}\}$ is the point load acting at any particular point on the beam. Further, Q^ϕ and Q^ψ represent the surface electric charge density and magnetic charge density, respectively.

The total potential energy is minimized by setting the first variation of Eq. (8) to zero

$$\begin{aligned}T_p = &\frac{1}{2}\sum_{k=1}^{N}\int_{\Omega^k}\delta\{\varepsilon^k\}^T\{\sigma^k\}d\Omega^k - \frac{1}{2}\sum_{k=1}^{N}\int_{\Omega^k}\delta[E^k]^T\{D^k\}d\Omega^k \\ &-\frac{1}{2}\sum_{k=1}^{N}\int_{\Omega^k}\delta[H^k]^T\{B^k\}d\Omega^k\int_A\delta\{d_t\}^T\{F_{surface}\}dA \\ &-\int_{\Omega^k}\delta\{d_t\}^T\{F_{body}\}d\Omega^k - \delta\{d_t\}^T\{F_{conc}\} \\ &-\int_A\delta\phi Q^\phi dA - \int_A\delta\psi Q^\psi dA = 0\end{aligned} \tag{9}$$

By substituting Eq. (1) into Eq. (9), we obtain

$$
\begin{aligned}
T_p^e = {} & \tfrac{1}{2}\sum_{k=1}^{N}\int_{\Omega^k}\delta\{\varepsilon^k\}^T[C_{V_f}^k]\{\varepsilon^k\}d\Omega^k - \tfrac{1}{2}\sum_{k=1}^{N}\int_{\Omega^k}\delta\{\varepsilon^k\}^T[e_{V_f}^k]\left\{E^k\right\}d\Omega^k - \tfrac{1}{2}\sum_{k=1}^{N}\int_{\Omega^k}\delta\{\varepsilon^k\}^T[q_{V_f}^k]\left\{H^k\right\}d\Omega^k, \\
& -\tfrac{1}{2}\sum_{k=1}^{N}\int_{\Omega^k}\delta\{\varepsilon^k\}^T[C_{V_f}^k]\left\{\alpha_{V_f}^k\right\}\Delta T d\Omega^k - \tfrac{1}{2}\sum_{k=1}^{N}\int_{\Omega^k}\delta\left\{E^k\right\}^T[e_{V_f}^k]^T\{\varepsilon^k\}d\Omega^k - \tfrac{1}{2}\sum_{k=1}^{N}\int_{\Omega^k}\delta\left\{E^k\right\}^T[\eta_{V_f}^k]\left\{E^k\right\}d\Omega^k, \\
& -\tfrac{1}{2}\sum_{k=1}^{N}\int_{\Omega^k}\delta\left\{E^k\right\}^T[m_{V_f}^k]\left\{H^k\right\}d\Omega^k - \tfrac{1}{2}\sum_{k=1}^{N}\int_{\Omega^k}\delta\left\{E^k\right\}^T\left\{p_{V_f}^k\right\}\Delta T d\Omega^k - \tfrac{1}{2}\sum_{k=1}^{N}\int_{\Omega^k}\delta\left\{H^k\right\}^T[q_{V_f}^k]^T\{\varepsilon^k\}d\Omega^k, \\
& -\tfrac{1}{2}\sum_{k=1}^{N}\int_{\Omega^k}\delta\left\{H^k\right\}^T[m_{V_f}^k]\left\{E^k\right\}d\Omega^k - \tfrac{1}{2}\sum_{k=1}^{N}\int_{\Omega^k}\delta\left\{H^k\right\}^T[\mu_{V_f}^k]\left\{H^k\right\}d\Omega^k - \tfrac{1}{2}\sum_{k=1}^{N}\int_{\Omega^k}\delta\left\{H^k\right\}^T\left\{\tau_{V_f}^k\right\}\Delta T d\Omega^k, \\
& -\int_A\delta\{d_t\}^T\{F_{surface}\}dA - \int_{\Omega^k}\delta\{d_t\}^T\{F_{body}\}d\Omega^k - \delta\{d_t\}^T\{F_{conc}\} - \int_A\delta\{\phi\}Q^\phi dA - \int_A\delta\{\psi\}Q^\psi dA
\end{aligned}
\tag{10}
$$

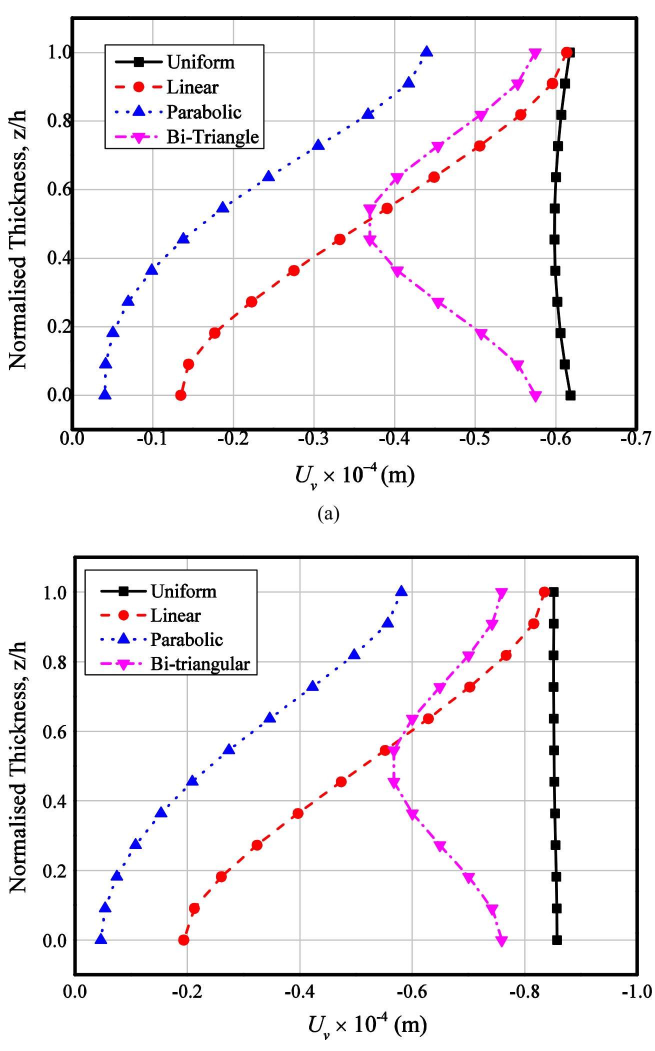

Fig. 12. Effect of various through thickness varying temperature profiles on longitudinal *y*-direction displacement component U_v (a) SFG-BFB (b) SFG-FBF.

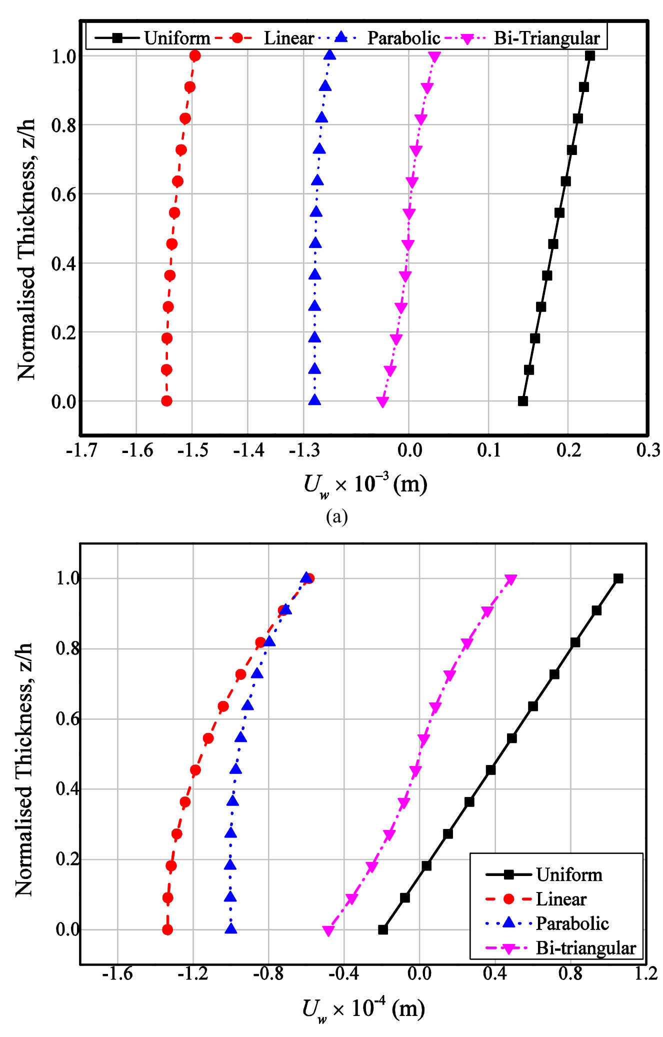

Fig. 13. Effect of various through thickness varying temperature profiles on *z*-direction displacement component U_w (a) SFG-BFB (b) SFG-FBF.

Substituting Eq. (6) into Eq. (9), we get

$$
\begin{aligned}
T_p^e = {} & \tfrac{1}{2}\sum_{k=1}^{N}\int_{\Omega^k}\delta\{d_t^e\}^T[B_t]^T[C_{V_f}^k][B_t]\{d_t^e\}d\Omega^k - \tfrac{1}{2}\sum_{k=1}^{N}\int_{\Omega^k}\delta\{d_t^e\}^T[B_t]^T[e_{V_f}^k][B_\phi]\{\phi^e\}d\Omega^k \\
& -\tfrac{1}{2}\sum_{k=1}^{N}\int_{\Omega^k}\delta\{d_t^e\}^T[B_t]^T[q_{V_f}^k][B_\psi]\{\psi^e\}d\Omega^k - \tfrac{1}{2}\sum_{k=1}^{N}\int_{\Omega^k}\delta\{d_t^e\}^T[B_t]^T[C_{V_f}^k]\left\{\alpha_{V_f}^k\right\}\Delta T d\Omega^k \\
& -\tfrac{1}{2}\sum_{k=1}^{N}\int_{\Omega^k}\delta\{\phi^e\}^T[B_\phi]^T[e_{V_f}^k]^T[B_t]\{d_t^e\}d\Omega^k - \tfrac{1}{2}\sum_{k=1}^{N}\int_{\Omega^k}\delta\{\phi^e\}^T[B_\phi]^T[\eta_{V_f}^k][B_\phi]\{\phi^e\}d\Omega^k \\
& -\tfrac{1}{2}\sum_{k=1}^{N}\int_{\Omega^k}\delta\{\phi^e\}^T[B_\phi]^T[m_{V_f}^k][B_\psi]\{\psi^e\}d\Omega^k - \tfrac{1}{2}\sum_{k=1}^{N}\int_{\Omega^k}\delta\{\phi^e\}^T[B_\phi]^T\left\{p_{V_f}^k\right\}\Delta T d\Omega^k \\
& -\tfrac{1}{2}\sum_{k=1}^{N}\int_{\Omega^k}\delta\{\psi^e\}^T[B_\psi]^T[q_{V_f}^k]^T[B_t]\{dt^e\}d\Omega^k - \tfrac{1}{2}\sum_{k=1}^{N}\int_{\Omega^k}\delta\{\psi^e\}^T[B_\psi]^T[m_{V_f}^k][B_\phi]\{\phi^e\}d\Omega^k \\
& -\tfrac{1}{2}\sum_{k=1}^{N}\int_{\Omega^k}\delta\{\psi^e\}^T[B_\psi]^T[\mu_{V_f}^k][B_\psi]\{\psi^e\}d\Omega^k - \tfrac{1}{2}\sum_{k=1}^{N}\int_{\Omega^k}\delta\{\psi^e\}^T[B_\psi]^T\left\{\tau_{V_f}^k\right\}\Delta T d\Omega^k \\
& -\int_A\delta\{d_t^e\}^T[N_t]^T\{F_{surface}\}dA - \tfrac{1}{2}\sum_{k=1}^{N}\int_{\Omega^k}\delta\{d_t^e\}^T[N_t]^T\{F_{body}\}d\Omega^k \\
& -\delta\{d_t^e\}^T[N_t]^T\{F_{conc}\} - \int_A\delta\{\phi^e\}[N_\phi]Q^\phi dA - \int_A\delta\{\psi^e\}[N_\psi]Q^\psi dA = 0
\end{aligned}
\tag{11}
$$

Upon simplication of these equations, we obtain

$$[K_{tt}^e]\{d_t^e\} + [K_{t\phi}^e]\{\phi^e\} + [K_{t\psi}^e]\{\psi^e\} = \{F_m^e\} + \{F_{th}^e\} \tag{12.a}$$

$$[K_{t\phi}^e]^T\{d_t^e\} - [K_{\phi\phi}^e]\{\phi^e\} - [K_{\phi\psi}^e]\{\psi^e\} = \{F_\phi^e\} - \{F_{p.e}^e\} \tag{12.b}$$

$$[K_{t\psi}^e]^T\{d_t^e\} - [K_{\phi\psi}^e]^T\{\phi^e\} - [K_{\psi\psi}^e]\{\psi^e\} = \{F_\psi^e\} - \{F_{p.m}^e\} \tag{12.c}$$

The various elemental stiffness matrices appearing in Eq. (12) are the elemental elastic stiffness matrix $[K_{tt}^e]$, the elemental electro-elastic coupling stiffness matrix $[K_{t\phi}^e]$, the elemental magneto-elastic coupling stiffness matrix $[K_{t\psi}^e]$, the elemental electric stiffness matrix $[K_{\phi\phi}^e]$, the elemental magnetic stiffness matrix $[K_{\psi\psi}^e]$, the elemental electro-magnetic stiffness matrix $[K_{\phi\psi}^e]$. The explicit forms of these matrices are given as follows:

$$
\begin{aligned}
&[K_{tt}^e] = \sum_{k=1}^{N}\{\textstyle\int_{\Omega^k}[B_t]^T[C_{V_f}^k][B_t]d\Omega^k\},\ [K_{t\phi}^e] = \sum_{k=1}^{N}\{\textstyle\int_{\Omega^k}[B_t]^T[e_{V_f}^k][B_\phi]d\Omega^k\}, \\
&[K_{t\psi}^e] = \sum_{k=1}^{N}\{\textstyle\int_{\Omega^k}[B_t]^T[q_{V_f}^k][B_\psi]d\Omega^k\},\ [K_{\phi\phi}^e] = \sum_{k=1}^{N}\{\textstyle\int_{\Omega^k}[B_\phi]^T[\eta_{V_f}^k][B_\phi]d\Omega^k\}, \\
&[K_{\phi\psi}^e] = \sum_{k=1}^{N}\{\textstyle\int_{\Omega^k}[B_\phi]^T[m_{V_f}^k][B_\psi]d\Omega^k\},\ [K_{\psi\psi}^e] = \sum_{k=1}^{N}\{\textstyle\int_{\Omega^k}[B_\psi]^T[\mu_{V_f}^k][B_\psi]d\Omega^k\}
\end{aligned}
\tag{13}
$$

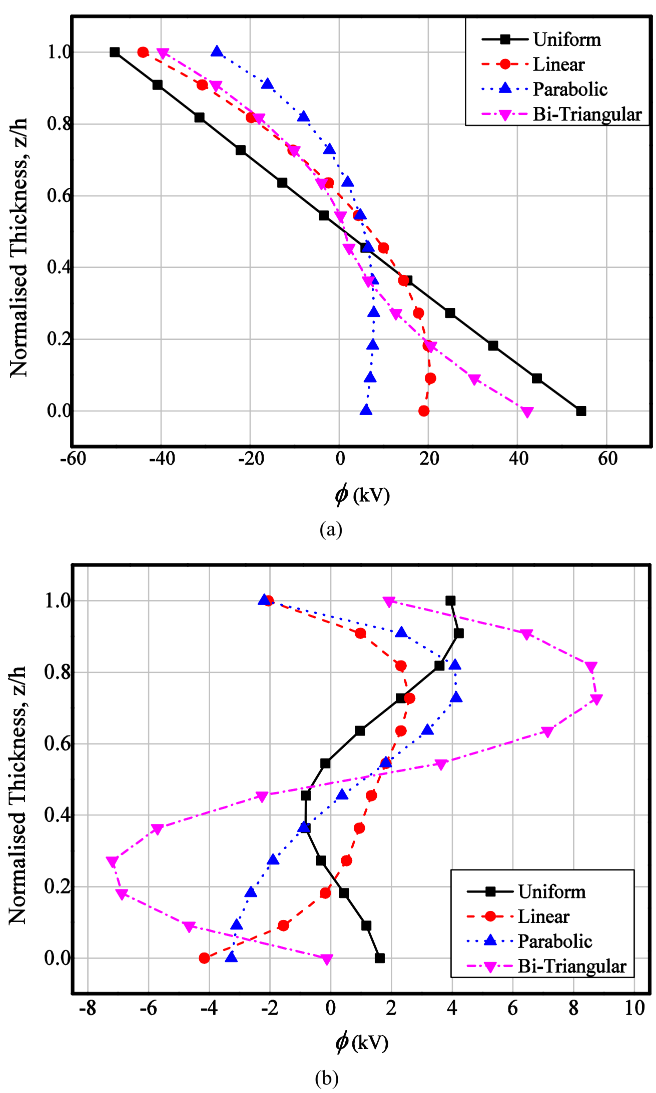

Fig. 14. Effect of various through thickness temperature profiles on electric potential (ϕ) (a) SFG-BFB (b) SFG-FBF.

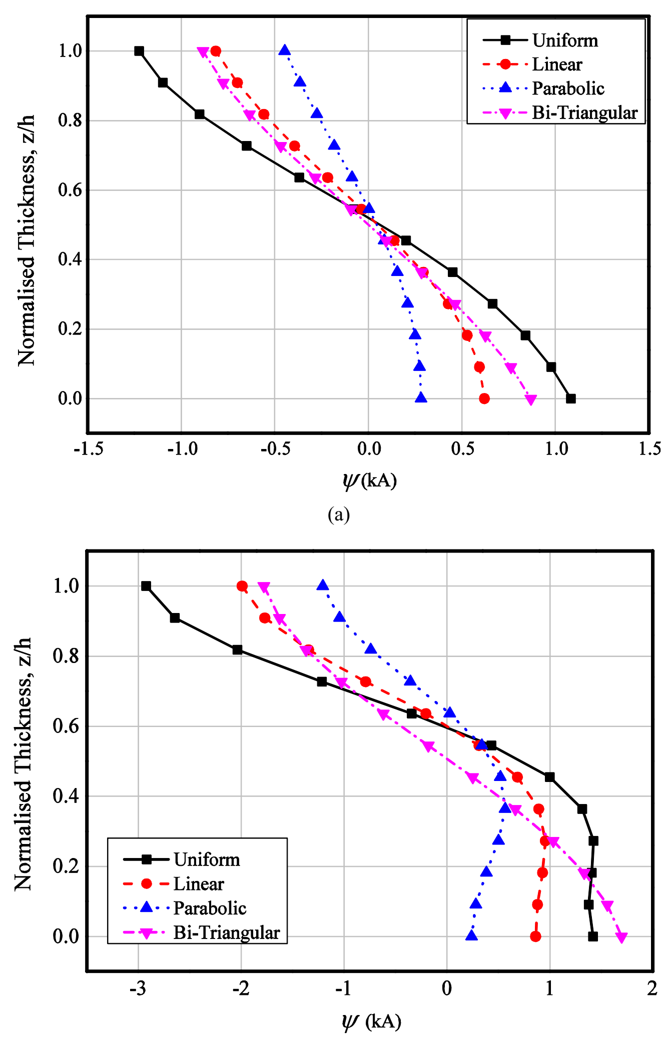

Fig. 15. Effect of various through thickness temperature profiles on magnetic potential (ψ) (a) SFG-BFB (b) SFG-FBF MEE beam.

Table 2
Effect of various cross-thickness temperature loads on the maximum electric potential (ϕ) of various types of MEE beam.

Through-thickness temperature profile	Max. Electric potential ϕ (kV)			
	BFB	SFG-BFB	FBF	SFG-FBF
Uniform	21.4	54.2	−7.7	4.22
Linear	−22.6	−44.1	−10.8	−4.16
Parabolic	−15.7	−27.4	−8.3	5.17
Bi-triangular	−16.4	42.2	5.6	8.53

Table 3
Effect of various cross-thickness temperature loads on the maximum magnetic potential (ψ) of various types of MEE beam.

Through-thickness temperature profile	Max. Magnetic potential ψ (A)			
	BFB	SFG-BFB	FBF	SFG-FBF
Uniform	656.2	1083.4	723.1	−2924.7
Linear	−498.6	−814.4	−582.3	−1991.3
Parabolic	−333.7	−446.3	−365.8	−1206.4
Bi-triangular	409.7	−882.4	532.3	−1779.2

Similarly, the various elemental load vectors appearing in Eq. (12) are the elemental mechanical load vector $\{F^e_m\}$, the elemental thermal load vector $\{F^e_{th}\}$, the elemental electric charge load vector $\{F^e_\phi\}$, the elemental magnetic load vector $\{F^e_\psi\}$, the elemental pyroelectric load vector $\{F^e_{p.e}\}$, the elemental pyromagnetic load vector $\{F^e_{p.m}\}$. The explicit form of the load vectors are given by

$$\{F^e_m\} = \int_{\Omega^k}[N_t]^T F_{body.e}\, d\Omega^k + \int_A [N_t]^T F_{surface}\, dA + [N_t]^T F_{conc.e}, \{F^e_\phi\} = \int_A [N_\phi]^T Q^\phi\, dA,$$
$$\{F^e_\psi\} = \int_A [N_\psi]^T Q^\Psi\, dA, \{F^e_{th}\} = \sum_{k=1}^{N}\left\{\int_{\Omega^k}[B_t]^T [C^k_{V_f}]\{\alpha^k_{V_f}\}\Delta T\, d\Omega^k\right\},$$
$$\{F^e_{p.e}\} = \sum_{k=1}^{N}\left\{\int_{\Omega^k}[B_\phi]^T\{p^k_{V_f}\}\Delta T\, d\Omega^k\right\}, \{Fp.m^e\} = \sum_{k=1}^{N}\left\{\int_{\Omega^k}[B_\psi]^T\{\tau^k_{V_f}\}\Delta T\, d\Omega^k\right\} \tag{14}$$

In the present analysis, the load vectors $\{F^e_m\}$, $\{F^e_\psi\}$ and $\{F^e_\phi\}$ are neglected. Hence, the Eq. (12) reduces to

$$[K^e_{tt}]\{d^e_t\} + [K^e_{t\phi}]\{\phi^e\} + [K^e_{t\psi}]\{\psi^e\} = \{F^e_{th}\} \tag{15.a}$$

$$[K^e_{t\phi}]^T\{d^e_t\} - [K^e_{\phi\phi}]\{\phi^e\} - [K^e_{\phi\psi}]\{\psi^e\} = \{F^e_{p.e}\} \tag{15.b}$$

$$[K^e_{t\psi}]^T\{d^e_t\} - [K^e_{\phi\psi}]^T\{\phi^e\} - [K^e_{\psi\psi}]\{\psi^e\} = \{F^e_{p.m}\} \tag{15.c}$$

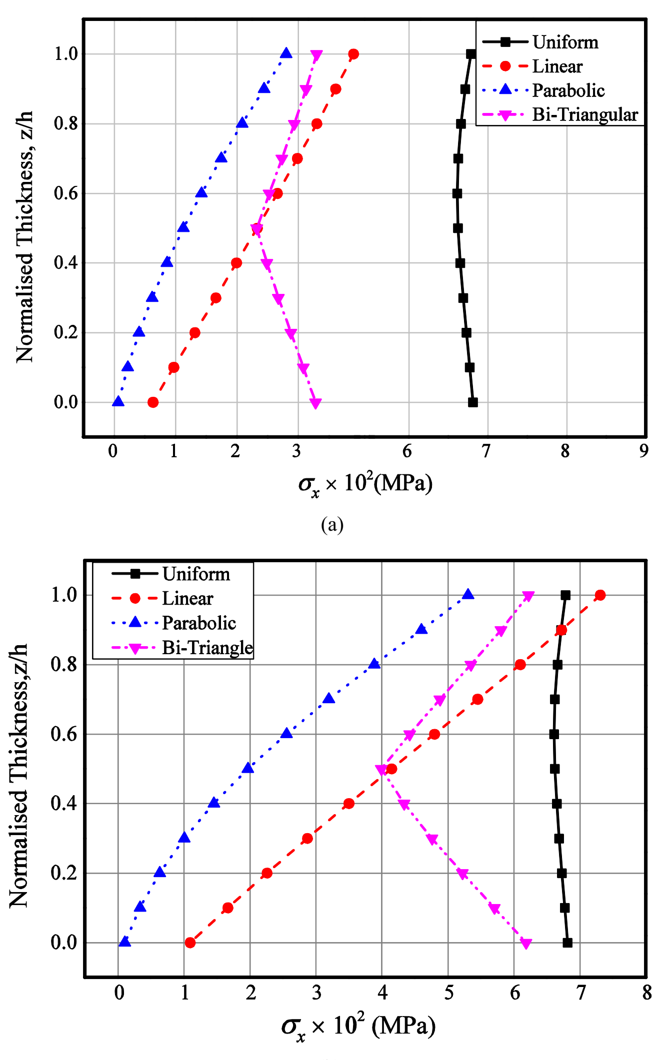

Fig. 16. Effect of through thickness temperature profiles on the variation of normal stress σ_x (a) SFG BFB (b) SFG-FBF MEE beam.

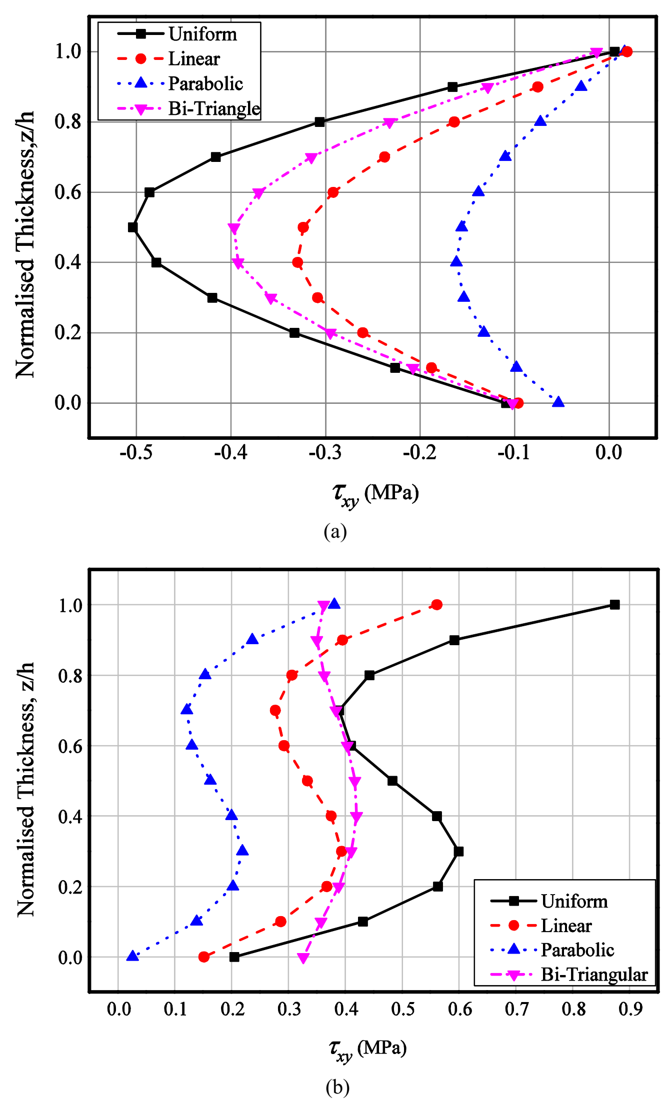

Fig. 17. Effect of through thickness temperature profiles on the variation of shear stress τ_{xy} (a) SFG-BFB (b) SFG-FBF MEE beam.

The condensation procedure is applied to Eq. 15.(a)–(c) and the nodal thermal displacements, electric and magnetic potentials are computed. Using Eq. (15.c) and solving for $\{\psi^e\}$ we obtain

$$\{\psi^e\} = [K^e_{\psi\psi}]^{-1}[K^e_{t\psi}]^T\{d^e_t\} - [K^e_{\psi\psi}]^{-1}[K^e_{\phi\psi}]^T\{\phi^e\} - [K^e_{\psi\psi}]^{-1}\{F^e_{p.m}\} \tag{16}$$

Substituting Eq. (16) in Eq. (15.b) and solving for $\{\phi^e\}$, we get

$$\begin{aligned}
&[K_{t\phi}]^T\{d^e_t\} - [K_{\phi\phi}]\{\phi\} - [K_{\phi\psi}][[K_{\psi\psi}]^{-1}[K_{t\psi}]^T\{d_t\} - [K_{\psi\psi}]^{-1}[K_{\phi\psi}]^T\{\phi\} - [K_{\psi\psi}]^{-1}\{F_{p.m}\}] = \{F_{p.e}\}\\
&\{d_t\}[[K_{t\phi}]^T - [K^e_{\phi\psi}][K_{\psi\psi}]^{-1}[K_{t\psi}]^T] - \{\phi\}[[K_{\phi\phi}] - [K_{\phi\psi}][K_{\psi\psi}]^{-1}[K_{\phi\psi}]^T] + [K_{\phi\psi}][K_{\psi\psi}]^{-1}\{F_{p.m}\} = \{F_{p.e}\}\\
&[K_1]\{d_t\} - [K_2]\{\phi\} = \{F_{p.e}\} - [K_{\phi\psi}][K_{\psi\psi}]^{-1}\{F_{p.m}\}, [K_1]\{d_t\} - [K_2]\{\phi\} = \{F_{\phi_sol}\},\\
&\{\phi\} = [K_2]^{-1}[K_1]\{d_t\} - [K_2]^{-1}\{F_{\phi_sol}\}
\end{aligned} \tag{17}$$

Further, on substituting Eqs. (16) and (17) in Eq. (15.a), we obtain

$$\begin{aligned}
&[K_{tt}]\{d_t\} + [K_{t\phi}]\{\phi\} + [K_{t\psi}]\Big[[K_{\psi\psi}]^{-1}[K_{t\psi}]^T\{d_t\} - [K_{\psi\psi}]^{-1}[K_{\phi\psi}]^T\{\phi\} - [K_{\psi\psi}]^{-1}\{F_{p.m}\}\Big] = \{F_{th}\},\\
&\{d_t\}[[K_{tt}] + [K_{t\psi}][K_{\psi\psi}]^{-1}[K_{t\psi}]^T] + \{\phi\}[[K_{t\phi}] - [K_{t\psi}][K_{\psi\psi}]^{-1}[K_{\phi\psi}]^T] - [K_{t\psi}][K_{\psi\psi}]^{-1}\{F_{p.m}\} = \{F_{th}\},\\
&[K_5]\{d_t\} + [K_6]\{\phi\} - [K_{t\psi}][K_{\psi\psi}]^{-1}\{F_{p.m}\} = \{F_{th}\},\\
&[K_5]\{d_t\} + [K_6][[K_3]\{d_t\} - [K_2]^{-1}\{F_{\phi_sol}\}] - [K_{t\psi}][K_{\psi\psi}]^{-1}\{F_{p.m}\} = \{F_{th}\},\\
&[[K_5] + [K_6][K_3]]\{d_t\} - [K_6][K_2]^{-1}\{F_{p.e}\} + [[K_6][K_4] - [[K_{t\psi}][K_{\psi\psi}]^{-1}]]\{F_{p.m}\} = \{F_{th}\},\\
&[K_7]\{d_t\} = [K_6][K_2]^{-1}\{F_{p.e}\} + [[K_{t\psi}][K_{\psi\psi}]^{-1} - [K_6][K_4]]\{F_{p.m}\} + \{F_{th}\},\\
&[K_7]\{d_t\} = [K_8]\{F_{p.e}\} + [K_9]\{F_{p.m}\} + \{F_{th}\}, [K_{eq}]\{d_t\} = \{F_{eq}\}
\end{aligned} \tag{18}$$

The component matrices and the equivalent force vectors constituting the Eqs. (17) and (18) are as follows:

$$\begin{aligned}
&[K_1] = [K_{\phi t}] - [K_{\psi\phi}][K_{\psi\psi}]^{-1}[K_{\psi t}], [K_2] = [K_{\phi\phi}] - [K_{\psi\phi}][K_{\psi\psi}]^{-1}[K_{\phi\psi}], [K_3] = [K_2]^{-1}[K_1]\\
&[K_4] = [K_2]^{-1}[K_{\psi\phi}][K_{\psi\psi}], [K_5] = [K_{tt}] + [K_{t\psi}][K_{\psi\psi}]^{-1}[K_{\psi t}][K_6] = [K_{t\phi}] - [K_{t\psi}][K_{\psi\psi}]^{-1}[K_{\phi\psi}],\\
&[K_7] = [K_5] + [K_6][K_3], [K_8] = [K_6][K_2]^{-1}, [K_9] = [K_{t\psi}][K_{\psi\psi}]^{-1} - [K_6][K_4],\\
&[K_{eq}] = [K_7], [K_{1_\psi}] = [K_{\psi t}] - [K_{\psi\phi}][K_3], [K_{2_\psi}] = [K_{\psi\psi}]^{-1}[K_{\psi\phi}][K_2]^{-1},\\
&[K_{3_\psi}] = [K_{\psi\psi}]^{-1}[K_{\psi\phi}][K_2]^{-1}[K_{\psi\phi}]^T[K_{\psi\psi}]^{-1} + [K_{\psi\psi}]^{-1},\\
&\{F_{eq}\} = [K_9]\{F_{p.m}\} + [K_8]\{F_{p.e}\} + \{F_{th}\}, \{F_{\phi_sol}\} = \{F_{p.e}\} - [K_{\psi\phi}]^T[K_{\psi\psi}]^{-1}\{F_{p.m}\}
\end{aligned} \tag{19}$$

3. Results and discussion

The finite element model derived in the previous section has been incorporated for the static analysis of stepped functionally graded magneto-electro-elastic beam (SFG-MEE). The material properties of each layer of the beam are assigned using the volume fractions of $BaTiO_3$ and $CoFe_2O_4$. The FE model is developed using 3D brick element. The variations of the direct quantities (displacements and potentials) and derived quantities (stresses, electric displacement and magnetic flux density) across the thickness of SFG-MEE beam in different thermal environment are computed.

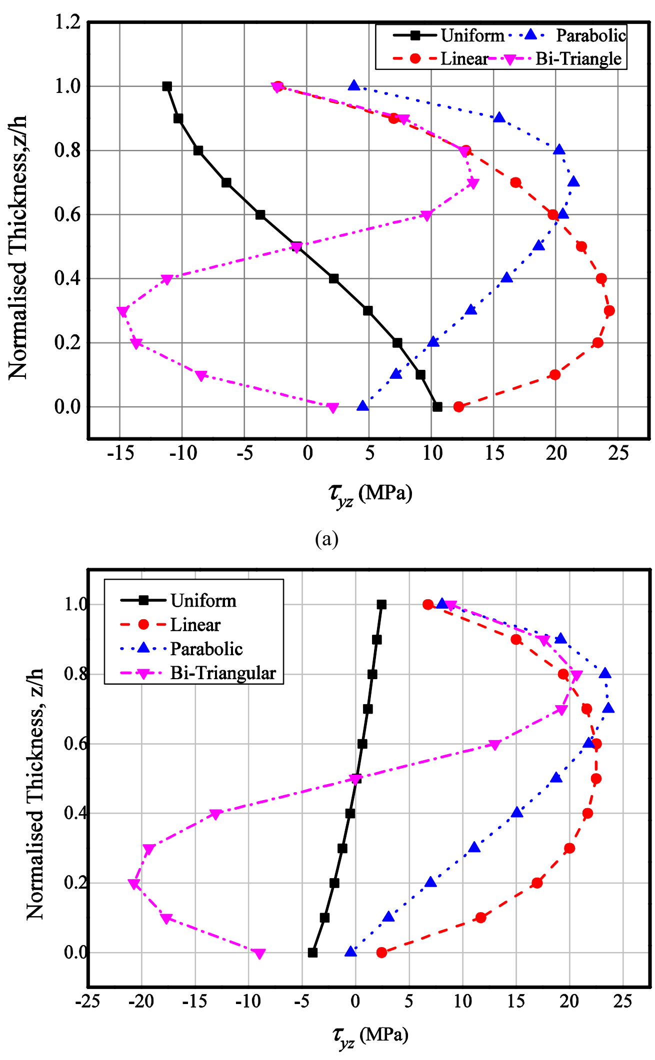

Fig. 18. Effect of through thickness temperature profiles on the variation of shear stress τ_{yz} (a) SFG-BFB (b) SFG-FBF MEE beam.

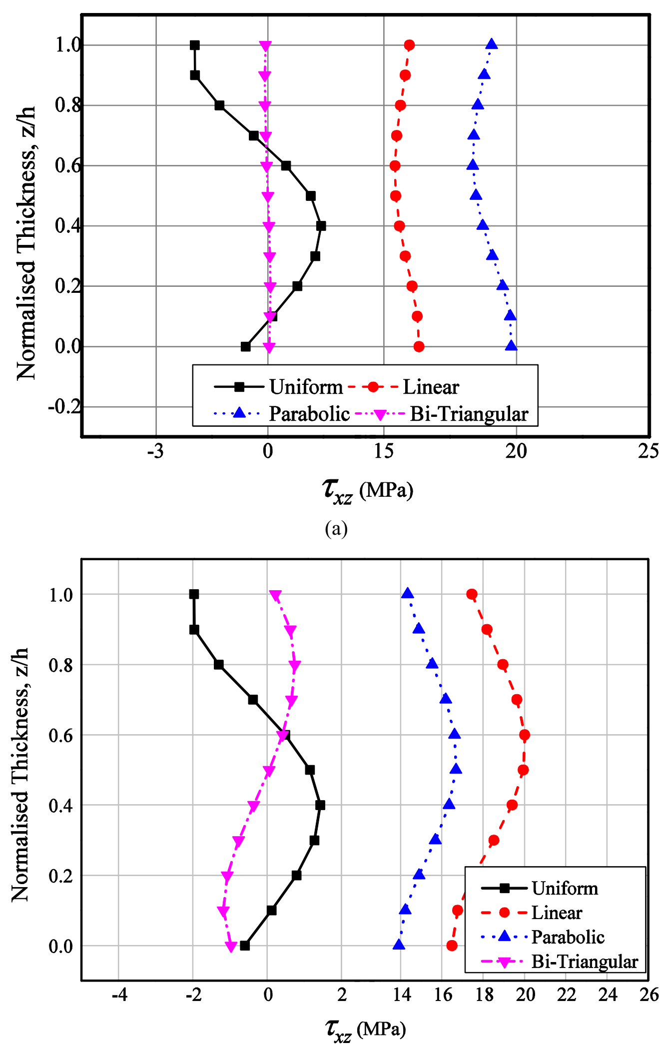

Fig. 19. Effect of through thickness temperature profiles on the variation of shear stress τ_{xz} (a) SFG-BFB (b) SFG-FBF MEE beam.

Few of the commonly encountered in-plane and through thickness temperature distributions are considered for the analysis. In addition, the effect of stacking sequence with respect to SFG-BFB and SFG-FBF MEE beam are evaluated. A novel attempt has been made to understand comprehensively the influence of pyroeffects on the multilayered MEE beam. The variations of the direct quantities and derived quantities at different regions of the beam are also investigated.

3.1. Validation of the present FE model

The results obtained from the present finite element (FE) formulation of the multilayered MEE beam is validated with the results summarized by Kondaiah et al. [28]. In order to justify the present formulation, the multilayered FE model is degenerated into a single layer. All the layers of the SFG-MEE beam is assigned with the material properties corresponding to the volume fraction $V_f = 0.5$ as tabulated in Table 1. The beam geometry, thermal loading and the boundary conditions are considered identical to those considered by Kondaiah et al. [28]. In order to obtain accurate results, mesh size is varied along the thickness direction and convergence study has been carried out. Fig. 3 depicts the convergence of the transverse z-direction displacement U_w with the mesh refinement. It may be observed from this figure that for the mesh size of 12 elements and 10 elements in the thickness and length direction, respectively a very good convergence is attained. Fig. 4 (a)–(e) illustrate the validation of the displacement, the electric potential and magnetic potential, respectively. It may be observed from these figures that the present results are in very good agreement with the results reported by Kondaiah et al. [28]. In order to validate further, the normal stresses (σ_x, σ_y and σ_z) and shear stresses (τ_{xy} and τ_{xz}) are also presented in Fig. 5(a)–(e). Similarly, the validation plots for electric displacement components (D_x, D_y and D_z) and magnetic flux density components (B_x, B_y and B_z) are shown in Figs. 6 and 7, respectively. It is evident from these figures that these results are also in excellent agreement with Kondaiah et al. [28].

3.2. In-plane temperature profiles

The various one dimensional temperature profiles varying along the length of the SFG-MEE beam are considered as follows.

3.2.1. Uniform temperature profile

The temperature of the SFG-MEE beam is uniformly raised from a stress free temperature T_0 to the final temperature T_{max}. For the

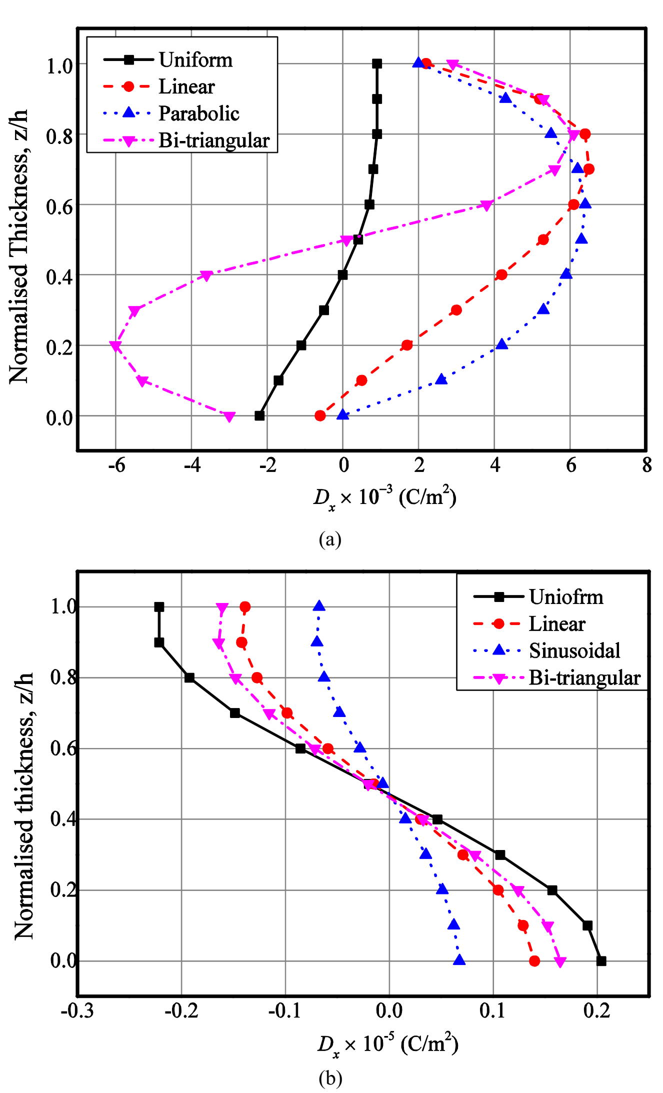

Fig. 20. Effect of through thickness temperature profiles on the variation of electric displacement D_x (a) SFG-BFB (b) SFG-FBF MEE beam.

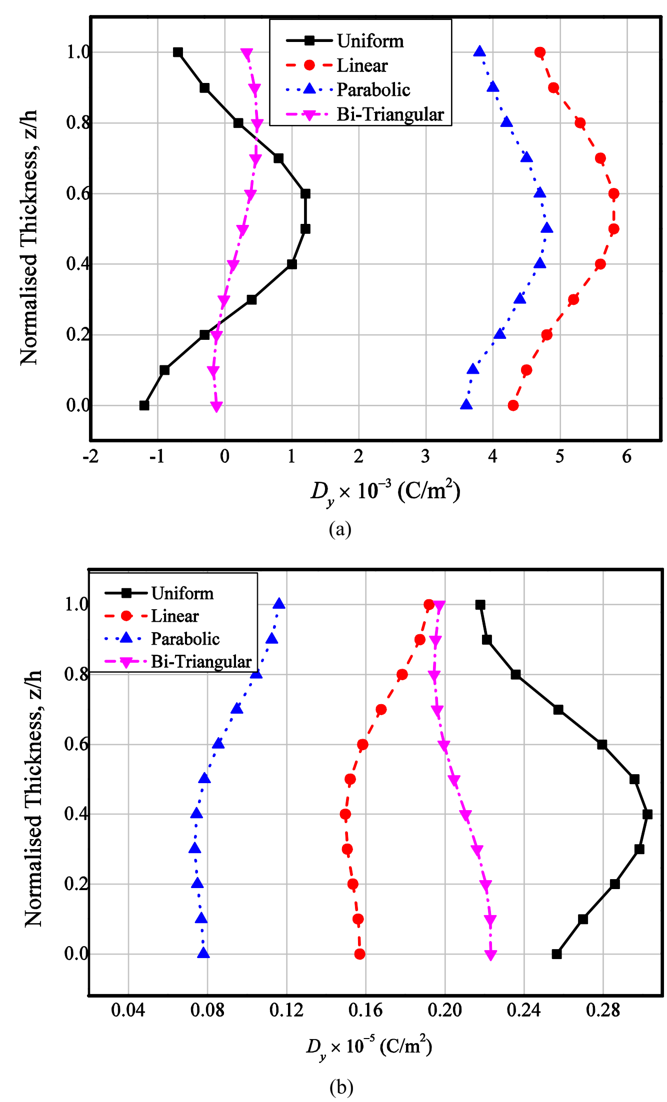

Fig. 21. Effect of through thickness temperature profiles on the variation of electric displacement D_y (a) SFG-BFB (b) SFG-FBF MEE beam.

ease of calculation, T_0 is assumed to be 0 K. The general temperature variation relation can be written as

$$\Delta T = T_{max} - T_0 \tag{20}$$

3.2.2. Half-sine temperature profile

The temperature of the SFG-MEE beam is assumed to vary along the beam length in a manner similar to a half sine wave with its peak at the midspan. The general equation corresponding to the half-sine temperature distribution can be written as

$$\Delta T = T_{max}\left\{\sin\left(\frac{\pi x}{L}\right)\right\} \quad 0 \leqslant x \leqslant L \tag{21}$$

in which, T_{max} is the maximum temperature, L is the beam length, x is the point of interest from the clamped end.

3.2.3. Linearly varying temperature profile

In this case, the static analysis of the SFG-MEE beam is carried out for linearly varying temperature load. The temperature distribution is such that it varies linearly along the beam length from an initial temperature (T_i) at clamped end of the beam to the maximum temperature (T_{max}) at the free end. The corresponding general equation may be expressed as

$$\Delta T = \{T_{max}\}x + \{T_i\} \quad 0 \leqslant x \leqslant L \tag{22}$$

3.3. Through-thickness temperature distribution

In the present analysis, different through thickness varying temperature profiles have been considered. The uniform temperature rise mentioned in Eq. (18) also fall under this category. The remaining temperature forms are encapsulated as follows.

3.3.1. Linear temperature profile

The temperature is assumed to vary linearly according to the general expression represented as follows:

$$\Delta T = T_i + T_{max}(z/h) \tag{23}$$

3.3.2. Bi-triangular temperature profile

The temperature of this profile follows a general trend of variation given by

$$\begin{aligned} \Delta T &= T_{max}(1-z) \quad 0 \leqslant z \leqslant h/2 \\ \Delta T &= T_{max}(z) \quad h/2 \leqslant z \leqslant h \end{aligned} \tag{24}$$

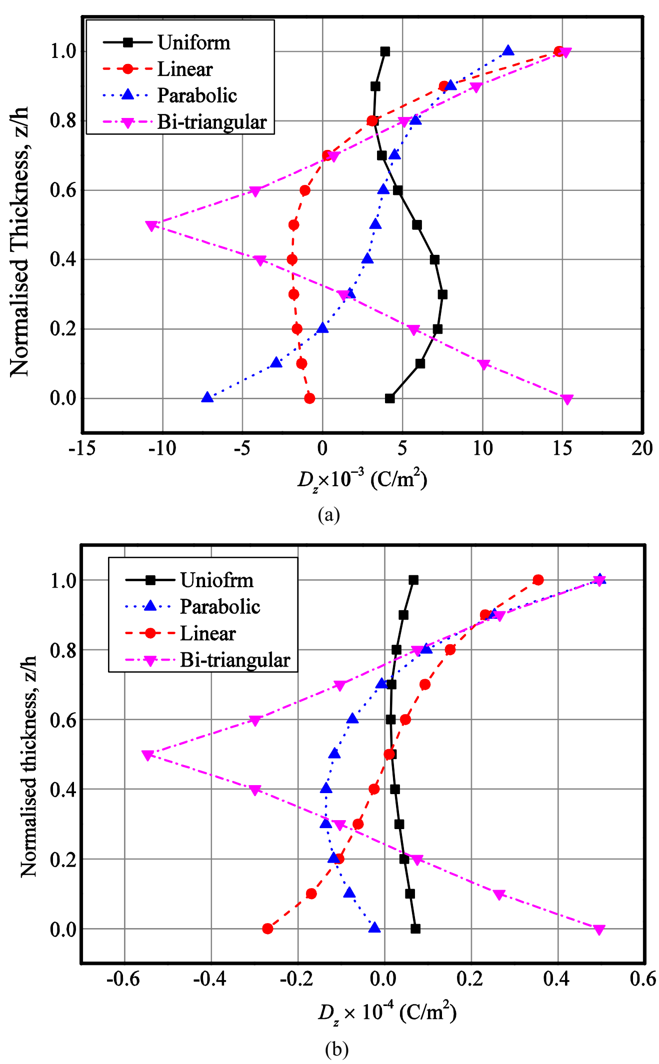

Fig. 22. Effect of through thickness temperature profiles on the variation of electric displacement D_z (a) SFG-BFB (b) SFG-FBF MEE beam.

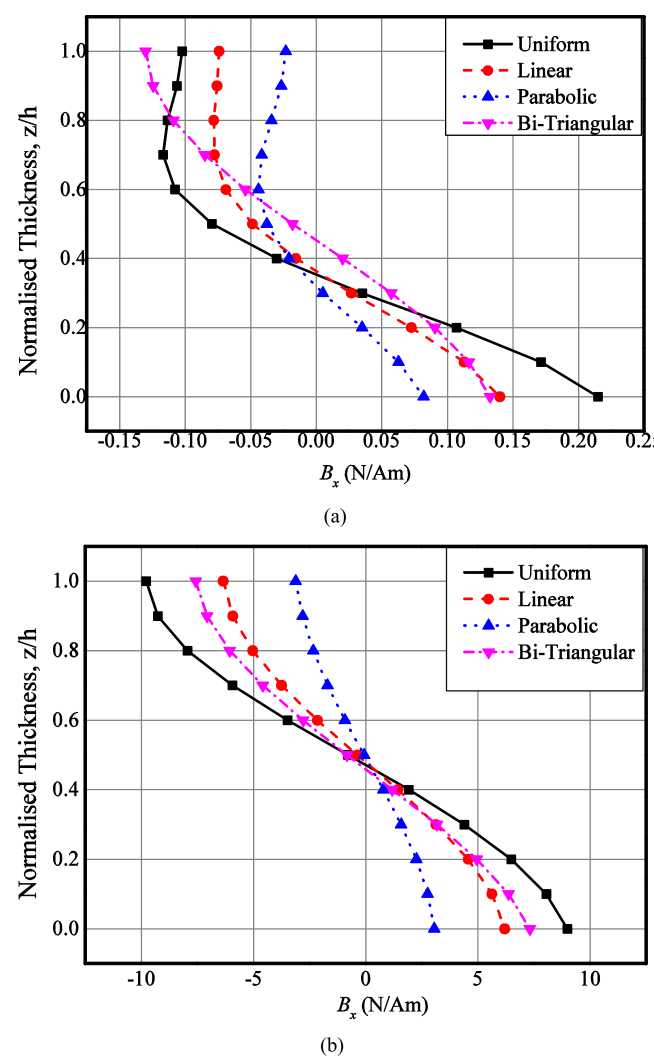

Fig. 23. Effect of through thickness temperature profiles on the variation of Magnetic flux density B_x (a) SFG-BFB (b) SFG-FBF MEE beam.

3.3.3. Parabolic temperature profile

The temperature distribution varying parabolically across the SFG-MEE beam thickness can be represented as follows:

$$\Delta T = T_{max}\left\{1 - \left(\frac{z}{h}\right)^2\right\} \quad 0 \leqslant z \leqslant h \tag{25}$$

In Eqs. (23)–(25), T_i is the temperature at the bottom layer of the beam, T_{max} is the maximum temperature, z is the distance of the point of interest from the bottom of the beam and h is the beam thickness.

3.4. Influence of pyro-effects

In this section, an attempt has been made to investigate the influence of pyroeffects on the direct quantities of the SFG-MEE beam. The term *Pyroeffects* generally refers to the thermo-electric and thermo-magnetic coupling generated due to different temperature profiles. In the present analysis, the study of pyroeffects is restricted to in-plane temperature distributions (Eqs. (20)–(22)). The values are obtained across the beam thickness at $x = L/2$. Fig. 8(a)–(e) demonstrate the variation of the direct quantities when the layerwise SFG-MEE beam subjected to uniform temperature rise of 100 K. Also, it emphasizes the effect of stacking sequence i.e. the layerwise SFG-BFB and SFG-FBF MEE beams. These figures also illustrate the influence of pyroeffects on the displacements and the potentials. It may be observed from these figures that the pyroeffects have a significant influence only on the electric potential of the SFG-MEE beam. In specific, the pyroeffects tends to improve the electric potential of the system whereas the negligible effect is observed for the displacements and magnetic potential. Fig. 8(a)–(c) suggest that the displacement components U_x, U_v and U_w are higher for the SFG-BFB stacking sequence then the SFG-FBF sequence of the MEE beam. This may be attributed to the lower stiffness of the BFB stacking sequence due to the presence of pure piezoelectric phase.

The numerical evaluation is carried out for the remaining in-plane temperature profiles *viz.* linear and sinusoidal temperature profiles. The variations of the direct quantities of the SFG-MEE beam subjected to linear temperature profile are illustrated in Fig. 9(a)–(e). It may be observed from Fig. 9(c) and (e) that the negligible effect of stacking sequence on the displacement component U_w and magnetic potential ψ, respectively. The variation of direct quantities for the SFG-MEE beam subjected to sinusoidal temperature profile is studied. From Fig. 10(a), the minimal influence of the pyroeffects on the longitudinal x-direction displacement component U_x of the SFG-MEE beam can be observed. Fig. 10(b) shows

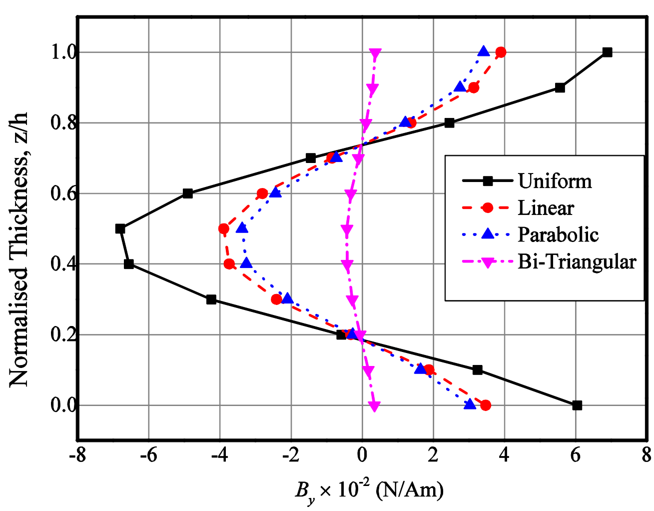

(a)

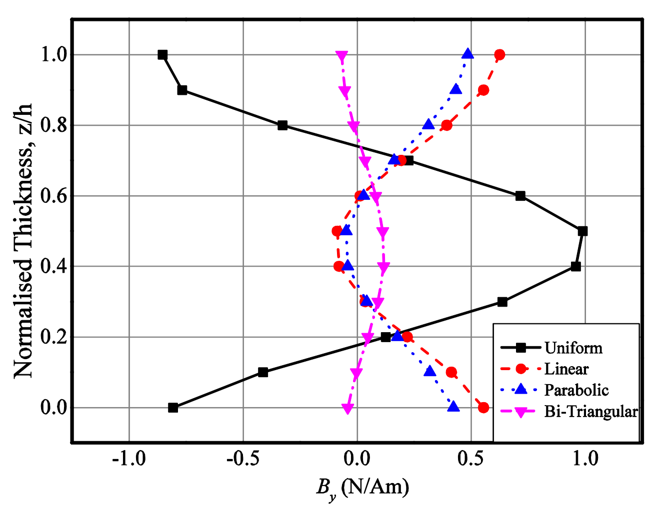

(b)

Fig. 24. Effect of through thickness temperature profiles on the variation of Magnetic flux density B_y (a) SFG-BFB (b) SFG-FBF MEE beam.

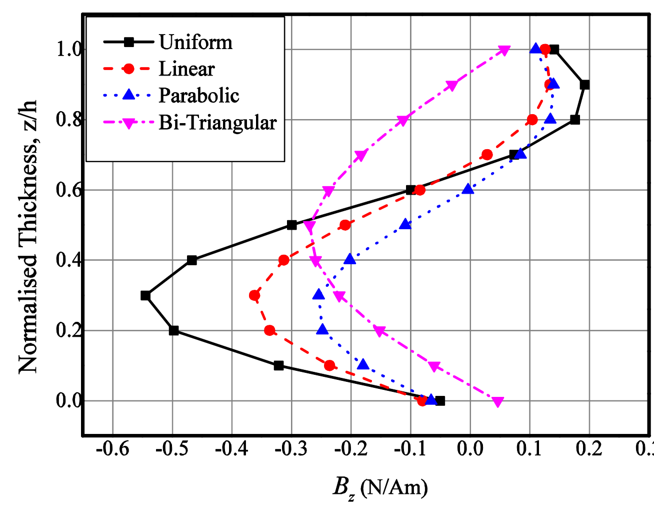

(a)

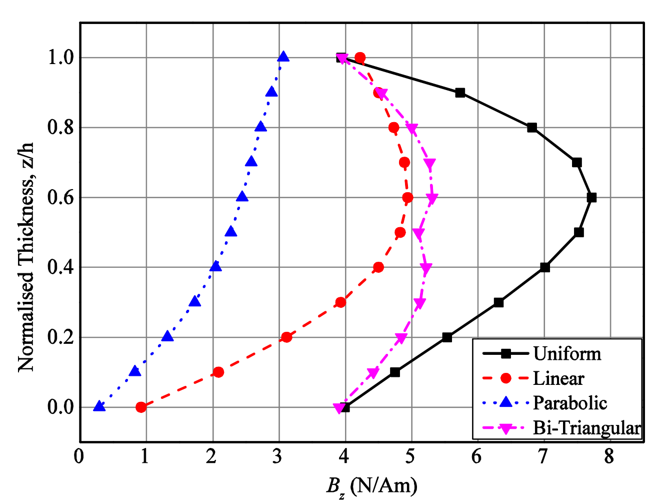

(b)

Fig. 25. Effect of through thickness temperature profiles on the variation of magnetic flux density B_z (a) SFG-BFB (b) SFG-FBF MEE beam.

the variation of longitudinal y-direction displacement component U_y. The variation of U_w, ϕ and ψ is shown in Fig. 10(c)–(e), respectively. It can be seen from Fig. 10(d) that the pyroeffects exhibit a

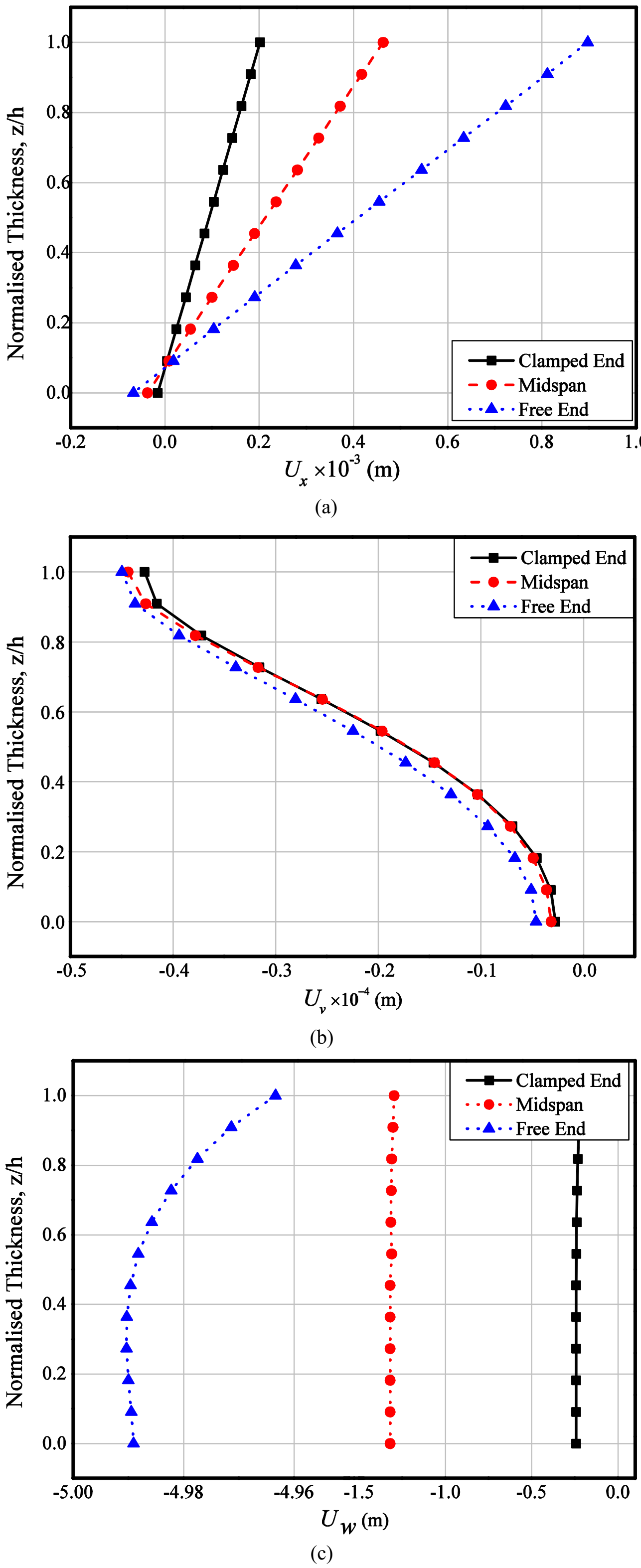

Fig. 26. Variations of (a) longitudinal x-direction displacement component U_x (b) y-direction displacement component U_y (c) z-direction displacement component U_w at different regions of the SFG-BFB MEE beam subjected to parabolically varying temperature.

noticeable influence on the electric potential while the SFG-BFB MEE beam exhibit the higher electric potential.

3.5. Effect of cross-thickness temperature profiles

For both the stacking sequence, the influence of temperature profiles (Eqs. (23)–(25)) on the longitudinal x-direction displacement component U_x, longitudinal y-direction displacement component U_y and transverse z-direction displacement component U_w of SFG-MEE beam is illustrated in Figs. 11–13, respectively. It can be seen that the uniform temperature profile have a predominant influence on the U_x and U_y whereas, the variations of these displacement components with respect to bi-triangular temperature profile is found insignificant. From Fig. 13(a) and (b) it can be observed that for both the stacking sequence, U_w is larger for linear temperature profile. Fig. 14(a) and (b) demonstrate the variation of the electric potential for SFG-BFB and SFG-FBF MEE beam, respectively. It is seen that for all the temperature profiles, SFG-BFB MEE beam has a higher electric potential than SFG-FBF MEE beam. This may be attributed to the presence of two pure piezoelectric layers in the stacking sequence. In addition, significant effect of uniform temperature distribution on the electric potential is observed for SFG-BFB MEE beam whereas, for the SFG-FBF MEE beam the electric potential is higher for bi-triangular temperature distribu-

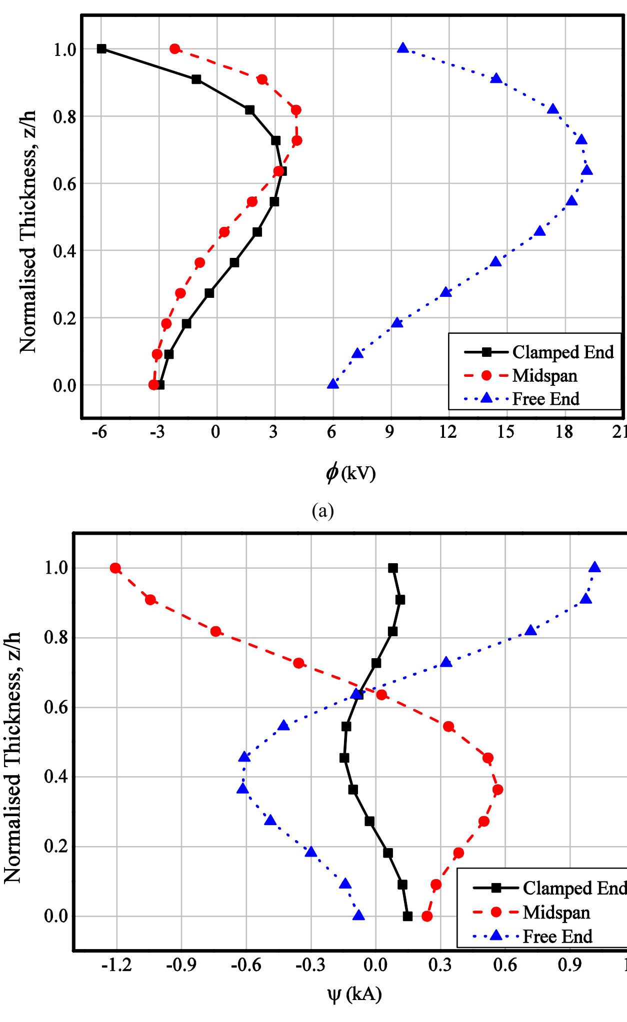

Fig. 27. Variations of (a) electric potential and (b) magnetic potential at different regions of the SFG-BFB MEE beam subjected to parabolically varying temperature.

tion. Similarly, Fig. 15(a)–(b) illustrate the magnetic potential distribution across the thickness of the beam. Since, SFG-FBF MEE beam has more pure piezomagnetic phase, this results into a higher magnetic potential than the SFG-BFB MEE beam. For both the stacking sequence, uniform temperature profile exhibits maximum magnetic potential. In addition, Tables 2 and 3 depict the comparison of the maximum electric potential and maximum magnetic potential of three layered MEE and SFG-MEE beam, respectively. It may be inferred from these tables that the SFG-MEE beam has a convincing effect over the normal MEE beam. Further, the numerical calculations are made to investigate the variation of derived quantities such as stresses, electric displacements and magnetic flux density. It is found that the normal stresses σ_y and σ_z follows a similar trend as that of the σ_x. Hence, for the sake of brevity, only the normal stress σ_x distribution is presented in Fig. 16(a) and (b) for SFG-BFB and SFG-FBF MEE beam, respectively. For uniform temperature profile, the variation in magnitude of the normal stress σ_x variation is minimal for both the stacking sequence while for the remaining temperature profiles SFB-FBF MEE beam higher than the SFB-BFB MEE beam. The shear stress τ_{xy} varies symmetrically across the mid-plane of the SFG-BFB MEE beam as shown in Fig. 17(a) whereas, for the SFG-FBF MEE beam, it varies anti-symmetrically as illustrated in Fig. 17(b). It can also be observed from this figure that the pure piezomagnetic phase ($V_f = 0.0$) in the corresponding stacking sequence experiences maximum τ_{xy} i.e. in case of SFG-BFB stacking sequence, the maximum shear stress τ_{xy} is witnessed at the middle layer whereas, in case of the SFG-FBF sequence, it is observed at the top or bottom layer of the beam. Further, except for the uniform temperature profile, τ_{yz} varies identically across the beam thickness for both the stacking sequence as shown in Fig. 18(a) and (b), respectively. Also, it can be observed that τ_{yz} follows the temperature distribution for parabolic and bi-triangular temperature profiles as shown in Fig. 19(a) and (b), respectively.

The electric displacement component in x-direction D_x with respect to SFG-BFB and SFG-FBF MEE beam is plotted in Fig. 20 (a) and (b), respectively. According to the constitutive equation (Eq. (1.b)), the magnitude of electric displacements mainly depend on the piezoelectric co-efficient matrix $[e]$ and dielectric coefficient matrix $[\eta]$. The higher value of these coefficients can be observed for pure piezoelectric ($V_f = 1.0$) phase (Table 1). Hence it is obvious that SFG-BFB MEE beam results in higher electric displacement. This holds good for D_y and D_z also, as shown in Figs. 21 (b) and 22(b), respectively. The significant effect of uniform temperature profile on the D_x and D_y of SFG-FBF MEE beam is observed.

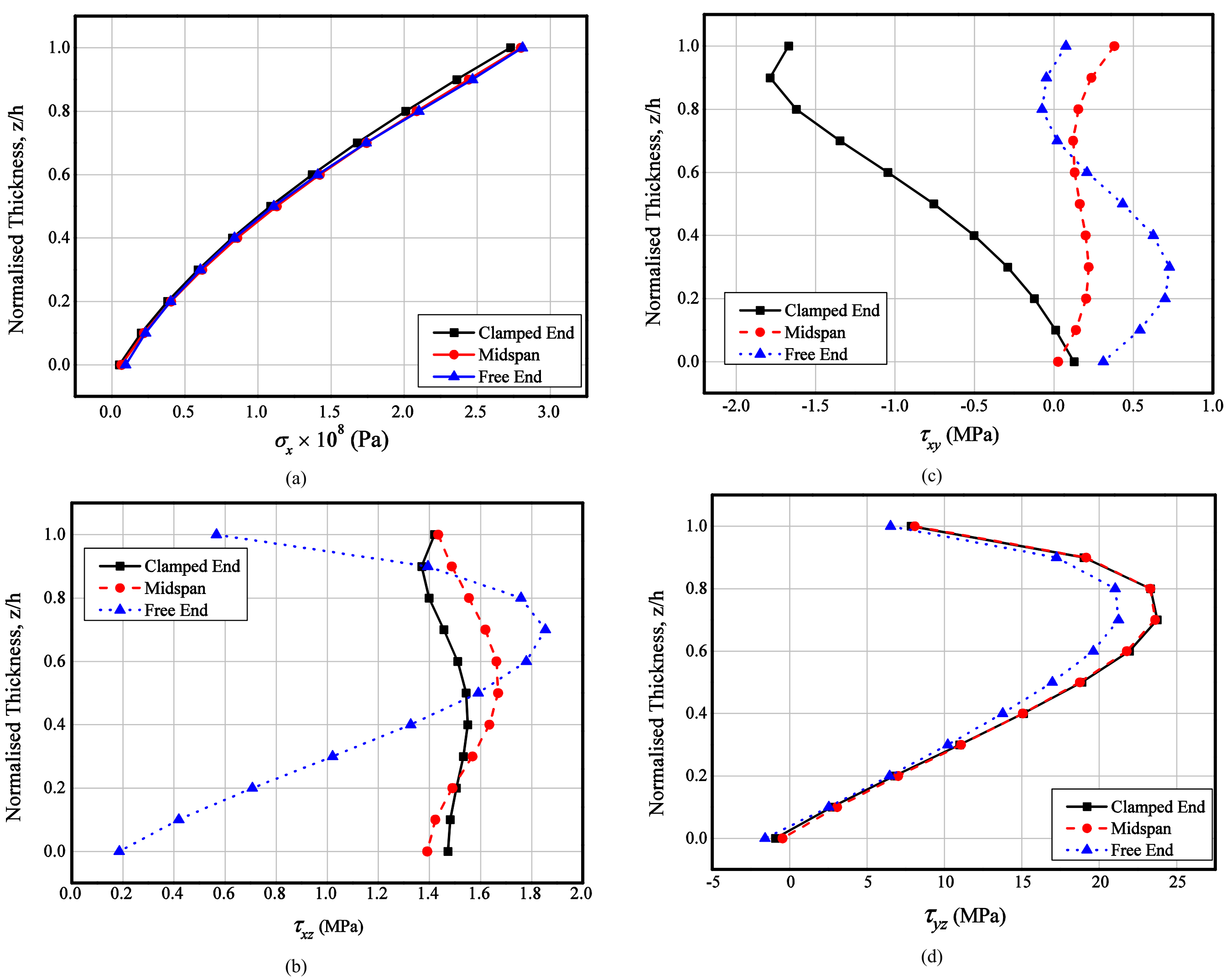

Fig. 28. Variations of (a) normal stress σ_x (b) shear stress τ_{xz} (c) shear stress τ_{xy} (d) shear stress τ_{yz} at different regions of SFG-BFB MEE beam subjected to parabolically varying temperature.

However, the bi-triangular temperature profile has a predominant effect on the D_z, for both the stacking sequences. Figs. 23–25 show the variation of magnetic flux density components B_x, B_y and B_z, respectively. As discussed earlier, the magnetic flux density is higher for SFG-FBF MEE beam because of the fact that the piezo-magnetic constant matrix [q] and magnetic permeability constant

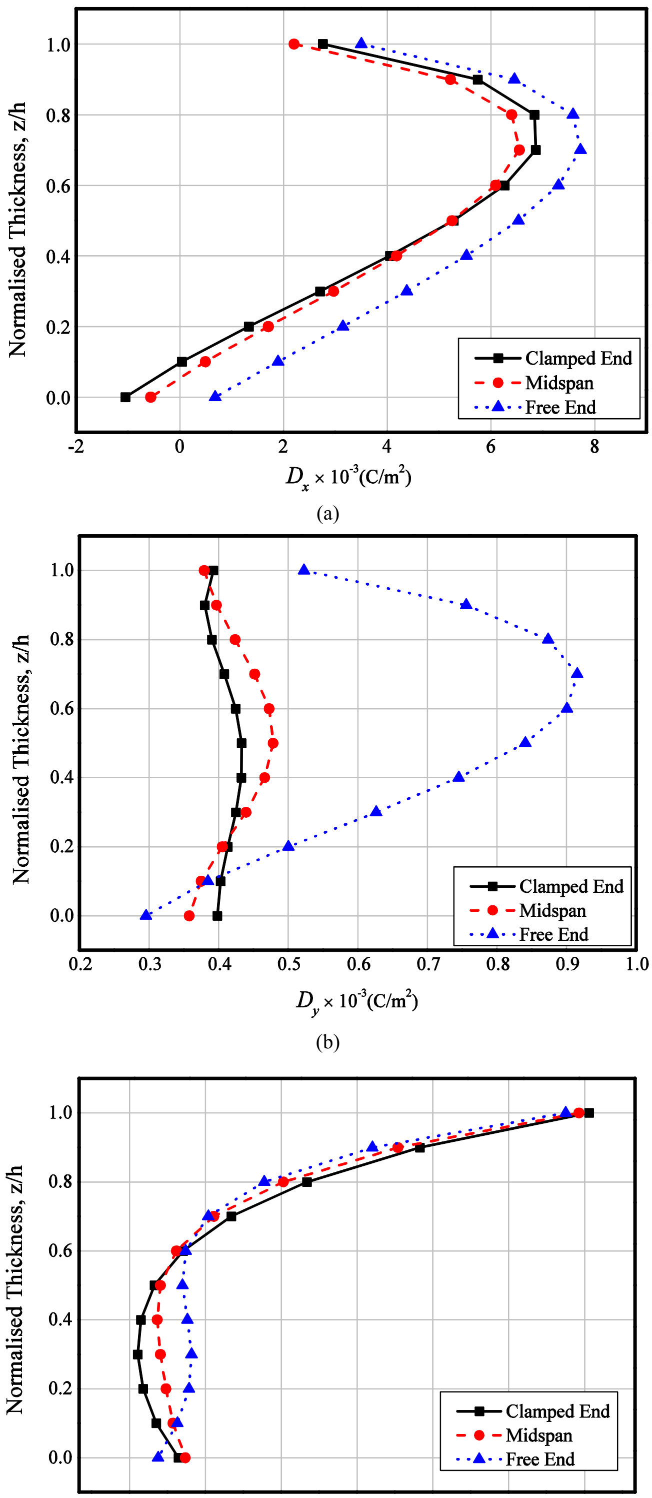

Fig. 29. Variations of electric displacement components (a) D_x (b) D_y (c) D_z at different regions of SFG-BFB MEE beam subjected to parabolically varying temperature.

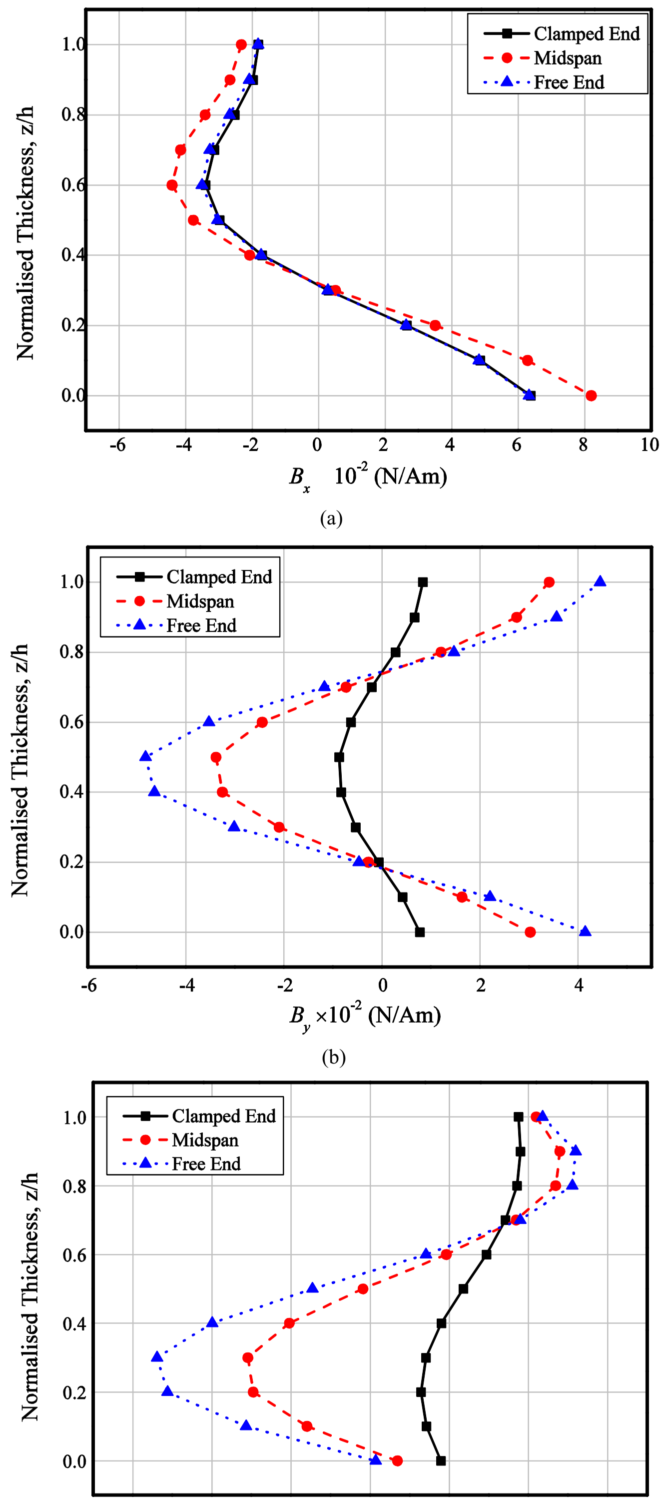

Fig. 30. Variations of magnetic flux density components (a) B_x (b) B_y (c) B_z at different regions of SFG-BFB MEE beam subjected to parabolically varying temperature.

matrix [μ] are higher for pure piezomagnetic phase. For both the stacking sequence the magnetic flux density components in all the three directions B_x, B_y and B_z are significantly influenced by uniform temperature profile as depicted in Figs. 23–25. The maximum value of B_y is observed at the midspan of the beam for all the temperature distributions.

3.6. Investigation at different beam region

In this section, the variations of the direct and derived quantities at different regions of the beam are investigated. The parabolically varying temperature distribution is considered in the present analysis. For the sake of brevity, the results are presented only for the BFB stacking sequence. The investigation points are chosen near the clamped end, at the midspan and at the free end of the beam. It may be observed from Fig. 26(a)–(c) that longitudinal x-direction displacement component U_x and transverse z-direction displacement component U_w are maximum at the free end whereas, a negligible discrepancies with respect to longitudinal y-direction displacement component U_v is observed at these regions. The electric potential is the maximum at the free end as depicted in Fig. 27(a) while the variation in the magnetic potential is illustrated in Fig. 27(b). It can be seen from Fig. 27(b) that near the clamped end, the variation of magnetic potential is minimal compared to other regions of the SFG-BFB MEE beam. The comparison of the stresses at different region of the beam is illustrated in Figs. 28(a)–(d). The normal stress σ_x shows an insignificant variation among the beam regions, as described in Fig. 28(a). From Fig. 28(b) and (c), a predominant effect of the free end and clamped end is observed on the shear stresses $\tau_{xz,}$ and τ_{xy}, respectively. The free end of the SFG-BFB MEE beam displays a higher magnitude of electric displacement components D_x and D_y as shown in Fig. 29 (a) and (b), respectively. Further, almost an identical variation of D_z is observed for all the beam regions as illustrated in Fig. 29(c). Further, from Fig. 30(a), it can be seen that at the midspan of the beam, a slightly higher magnetic flux density component B_x is witnessed whereas, the clamped end and free end almost have an equal flux distribution. From Fig. 30(b) and (c), it may be observed that the variation of B_y and B_z is greater at the free end of the SFG-BFB MEE beam.

4. Conclusions

In this article, a finite element (FE) formulation to analyze the static behavior of the multilayered stepped functionally graded magneto-electro-elastic (SFG-MEE) beam in different thermal environment is developed and implemented. Two different forms of temperature distributions i.e., in-plane and through thickness are considered. The cross-thickness variations of the direct quantities (displacements and potentials) and derived quantities (stresses, electric displacement and magnetic flux density) of the SFG-MEE beam are presented. The numerical study reveals that irrespective of the temperature profiles, only the electric potential is influenced by the pyroeffects. The displacement components are higher for SFB-BFB MEE beam whereas, SFG-FBF MEE beam have a predominant effect on the in-plane normal stresses. The maximum electric potential and hence the electric displacement components is observed for SFG-BFB MEE beam whereas, the maximum magnetic potential and magnetic flux density is noticed for SFG-FBF MEE beam. The reason is obvious due to increased number of pure piezoelectric and pure piezomagnetic layers in the corresponding stacking sequence. Among the different temperature profiles considered, the uniform temperature rise is witnessed to have a significant influence on the behavior of SFG-MEE beam. In addition, the variations of the direct quantities and derived quantities at different regions of the SFG-MEE cantilever beam are studied.

References

[1] Pan E, Heyliger H. Free vibrations of simply supported and multilayered magneto-electro-elastic plates. J Sound Vib 2002;252(3):429–42.
[2] Sladek J, Sladek V, Krahulec S, Pan E. The MLPG analyses of large deflections of magneto electro elastic plates. Eng Anal Boundary Elem 2013;37(4):673–82.
[3] Ramirez Fernando, Heyliger Paul R, Pan Ernian. Free vibration response of two-dimensional magneto-electro-elastic laminated plates. J Sound Vib 2006;292:626–44.
[4] Milazzo A, Orlando C, Alaimo A. An analytical solution for the magneto-electro-elastic bimorph beam forced vibrations problem. Smart Mater Struct 2009;18 (8):85012.
[5] Kattimani SC, Ray MC. Smart damping of geometrically nonlinear vibrations of magneto-electro-elastic plates. Compos Struct 2014;14:51–63.
[6] Kattimani SC, Ray MC. Active control of large amplitude vibrations of smart magneto-electro-elastic doubly curved shells. Int J Mech Mater Des 2014;10 (4):351–78.
[7] Kattimani SC, Ray MC. Control of geometrically nonlinear vibrations of functionally graded magneto-electro-elastic plates. Int J Mech Sci 2015;99:154–67.
[8] Rajesh Bhangale K, Ganesan N. Free vibration of simply supported functionally graded and layered magneto-electro-elastic plates by finite element method. J Sound Vib 2006;294:1016–38.
[9] Vaezi Mohamad, Shirbani Meisam Moory, Hajnayeb Ali. Free vibration analysis of magneto-electro-elastic microbeams subjected to magneto-electric loads. Physica E 2016;75:280–6.
[10] Xin Libo, Hu Zhendong. Free vibration of layered magneto-electro-elastic beams by SS-DSC Approach. Compos Struct 2015;125:96–103.
[11] Ray MC, Bhattacharya R, Samanta B. Static analysis of an intelligent structure by the finite element method. Comput Struct 1994;52:617–31.
[12] Garcia Lage R, Mota Soares CM, Mota Soares CA, Reddy JN. Layerwise partial mixed finite element analysis of magneto-electro-elastic plates. Comput Struct 2004;82:1293–301.
[13] Biju B, Ganesan N, Shankar K. Dynamic response of multiphase magnetoelectroelastic sensors using 3D magnetic vector potential approach. IEEE Sens J 2011;11(9):2169–76.
[14] Daga A, Ganesan N, Shankar K. Transient dynamic response of cantilever magneto-electro-elastic beam using finite elements. Int J Comput Methods Eng Sci Mech 2009;10(3):173–85.
[15] Chen WQ, Lee KY, Ding HJ. On free vibration of non-homogeneous transversely isotropic magneto-electro-elastic plates. J Sound Vib 2005;279: 237–51.
[16] Wang J, Chen L, Fang S. State vector approach to analysis of multilayered magneto-electro-elastic plates. Int J Solids Struct 2003;40(7):1669–80.
[17] Chen J, Chen H, Pan E, Heyliger PR. Modal analysis of magneto-electro-elastic plates using the state-vector approach. J Sound Vib 2007;304(3–5):722–34.
[18] Phoenix SS, Satsangi SK, Singh BN. Layer-wise modelling of magneto-electro-elastic plates. J Sound Vib 2009;324(3–5):798–815.
[19] Aboudi J. Micromechanical analysis of fully coupled electro-magneto-thermo-elastic multiphase composites. Smart Mater Struct 2001;10(5):867–77.
[20] Hadjiloizi DA, Georgiades AV, Kalamkarov AL, Jothi S. Micromechanical modeling of piezo-magneto-thermo-elastic composite structures: Part I Theory. Eur J Mech A Solids 2013;39:298–312.
[21] Hadjiloizi DA, Georgiades AV, Kalamkarov AL, Jothi S. Micromechanical modeling of piezo-magneto-thermo-elastic composite structures: Part 2-Applications. Eur J Mech A Solids 2013;39:313–27.
[22] Tang Tian, Yu Wenbin. Variational asymptotic homogenization of heterogeneous electromagnetoelastic materials. Int J Eng Sci 2008;46:741–57.
[23] Tang Tian, Yu Wenbin. Micromechanical modeling of the multiphysical behavior of smart materials using the variational asymptotic method. Smart Mater Struct 2009;18:125026.
[24] Sladek Jan, Sladek Vladimir, Krahulec Slavomir, Song Chongmin. Micromechanics determination of effective properties of voided magnetoelectroelastic materials. Comput Mater Sci 2016;116:103–12.
[25] Panda Satyajit, Ray MC. Nonlinear finite element analysis of functionally graded plates integrated with patches of piezoelectric fiber reinforced composite. Finite Elem Anal Des 2008;44:493–504.
[26] Kumaravel A, Ganesan N, Sethuraman R. Buckling and vibration analysis of layered and multiphase magneto-electro-elastic beam under thermal environment. Multidiscipline Model Mater Struct 2007;3(4):461–76.
[27] Kumaravel A, Ganesan N, Sethuraman R. Steady-state analysis of a three-layered electro-magneto-elastic strip in a thermal environment. Smart Mater Struct 2007;16(2):282–95.
[28] Kondaiah P, Shankar K, Ganesan N. Studies on magneto-electro-elastic cantilever beam under thermal environment. Coupled Syst Mech 2012;1 (2):205–17.
[29] Kondaiah P, Shankar K, Ganesan N. Pyroelectric and pyromagnetic effects on behavior of magneto-electro-elastic plate. Coupled Syst Mech 2013;2:1–22.
[30] Carrera Erasmo, Ciuffreda Angelo. Closed-form solutions to assess multilayered-plate theories for various thermal stress problems. J Therm Stresses 2004;27(11):1001–31.

[31] Sunar M, Ahmed Al-Garni Z, Ali MH, Kahraman R. Finite element modeling of thermopiezomagnetic smart structures. AIAA J 2002;40:1845–51.
[32] Badri Thar M, Al-Kayiem Hussain H. Analytical solution for simply supported and multilayered Magneto-Electro-Elastic Plates. Asian J Sci Res 2013;6:236–44.
[33] Tauchert TR. Cylindrical bending of hybrid laminates under thermo-electro-mechanical loading. J Therm Stresses 1996;19:287–96.
[34] Ebrahimi Farzad, Barati Mohammad Reza. Dynamic modeling of a thermo-piezo-electrically actuated nanosize beam subjected to a magnetic field. Appl Phys A 2016;122:451.
[35] Ebrahimi Farzad, Barati Mohammad Reza. Electromechanical buckling behavior of smart piezoelectrically actuated higher-order size-dependent graded nanoscale beams in thermal environment. Int J Smart Nano Mater 2016;7(2):69–90.